Universal scaling laws rule explosive growth in human cancers

Víctor M. Pérez-García[1]*, Gabriel F. Calvo[1], Jesús J. Bosque[1], Odelaisy León-Triana[1], Juan Jiménez[1], Julián Pérez-Beteta[1], Juan Belmonte-Beitia[1], Manuel Valiente[2], Lucía Zhu[2], Pedro García-Gómez[2], Pilar Sánchez-Gómez[3], Esther Hernández-San Miguel[3], Rafael Hortigüela[3], Youness Azimzade[4], David Molina-García[1], Álvaro Martínez[1,5], Ángel Acosta Rojas[6], Ana Ortiz de Mendivil[7], Francois Vallette[8], Philippe Schucht[9], Michael Murek[9], María Pérez-Cano[1], David Albillo[10], Antonio F. Honguero Martínez[11], Germán A. Jiménez Londoño[12], Estanislao Arana[13] & Ana M. García Vicente[12]

Most physical and other natural systems are complex entities composed of a large number of interacting individual elements. It is a surprising fact that they often obey the so-called scaling laws relating an observable quantity with a measure of the size of the system. Here we describe the discovery of universal superlinear metabolic scaling laws in human cancers. This dependence underpins increasing tumour aggressiveness, due to evolutionary dynamics, which leads to an explosive growth as the disease progresses. We validated this dynamic using longitudinal volumetric data of different histologies from large cohorts of cancer patients. To explain our observations we put forward increasingly-complex biologically-inspired mathematical models that captured the key processes governing tumor growth. Our models predicted that the emergence of superlinear allometric scaling laws is an inherently three-dimensional phenomenon. Moreover, the scaling laws thereby identified allowed us to define a set of metabolic metrics with prognostic value, thus providing added clinical utility to the base findings.

Biological systems display complex spatially and temporally varying structures that are mainly a consequence of their underlying metabolism. Organisms continuously incorporate energetic and material resources from the environment, transforming and allocating them into different compartments that allow for their growth, reproduction and, hence, survival, both as individuals and as species. Metabolism involves random fluctuations and hierarchical processes that determine the pace at which organisms live and evolve. In a semimal work [1], Kleiber observed that, for a broad variety of species, metabolic rates scale to the 3/4 power of the animal's mass. This result contradicted theories assuming a direct proportionality between the animal's volume and its metabolic rate, or other scalings such as metabolic rate being proportional to the animal surface. Scaling laws are of the form $Z = \alpha V^{\beta}$, where Z is an observable quantity, V is a measure of the size of the system -in living systems typically their volume or mass- α is a rate constant and β represents the scaling exponent [2]. West and coworkers proposed that the exponent $\beta = 3/4$ found by Kleiber could be the result of principles of minimal energy [3]. Many related studies have explored allometric scaling laws in other biological contexts [4–6].

Do human cancers obey metabolic scaling laws? Some evidence obtained from *in vitro* experiments or from xenotransplantation of patient-derived cells into immunocompromised mice seem to support that cancers also obey the Kleiber's law or similar sublinear dynamics [7–9]. However, no works have uncovered scalings laws from large cancer patient datasets. Here we addressed this question under the initial hypotheses that malignant tumours would scale between the metabolic requirements of coordinated tissues governed by minimal energy principles (leading to an exponent $\beta \simeq 3/4$) and that of independent uncoordinated units (exponent $\beta \simeq 1$).

Tumour cells exhibit high metabolic requirements to sustain an upregulated proliferation. Nutrients such as glucose and, to a lesser extent, glutamine are mostly used to fuel biomass formation and macromolecule synthesis [10]. Deregulated glucose uptake by tumour cells, known as the Warburg effect, constitutes the basis of positron-emission-tomography/computed-tomography (PET/CT)-based imaging by means of the radioactive tracer ^{18}F-fluorodeoxyglucose (^{18}F-FDG), widely used in clinical oncology [11]. To study the relationship between tumour metabolic rates and volume we collected data of different cancer types imaged at diagnosis with ^{18}F-FDG PET/CT. Tumours were segmented and their total lesion activity (TLA) and metabolic tumour volume (MTV) calculated. TLA and MTV were computed as the product of each voxel volume within the tumour by its measured standardized uptake value (SUV) and as the summed volume of the segmented tumour voxels, respectively. Our first goal was to determine whether a dependence of the form $\mathrm{TLA} \sim \alpha \mathrm{MTV}^{\beta}$ could be identified. Figure 1 shows log-log plots of MTV versus TLA for patients with: locally advanced breast cancer (LABC), head and neck cancer (H&NC, stages II-IV), non-small-cell lung cancer (NSCLC, stages I-III) and rectal cancer (RC, stages III-IV) (see 'Methods' for more patient data). The obtained exponents were, $\beta = 1.307 \pm 0.069$ ($R^2 = 0.874$, LABC), $\beta = 1.182 \pm 0.030$ ($R^2 = 0.954$, H&NC), $\beta = 1.248 \pm 0.032$ ($R^2 = 0.900$, NSCLC), $\beta = 1.386 \pm 0.152$ ($R^2 = 0.798$, RC), as shown in Fig. 1(a,b,d,e). Thus, superlinear scalings clustered around the rational number $\beta = 5/4$ (Fig. 1(g)). Moreover, all patients scanned in the same institution and undergoing an identical protocol, thus providing comparable data, followed a common scaling law with $\beta = 1.309 \pm 0.030$ ($R^2 = 0.895$) [Fig. 1(h)]. Possible artefacts on the scaling exponents due to the partial volume effect in PET images were discarded (see SI, Section S4). Our findings contradicted the hypothesis of metabolic scaling being sublinear suggesting a fundamentally different dynamics.

This superlinear glucose uptake could be the result of different mechanisms. The first one would be an increase of the Warburg phenotype leading to a less efficient use of glucose. Also, the presence of immune cells and inflammation within the tumour region could be a contributing factor. However, since glucose is mostly used to satisfy the proliferation demands [10, 11], we suspected that an increase of the proliferation rate with size was probably the main underlying cause.

To clarify this, we gathered data from glioma patients (grades II-IV) imaged at diagnosis with ^{18}F-Fluorocholine PET (^{18}F-FCHOL), and from breast cancer patients (stages II-IV) imaged at diagnosis with 3'-deoxy-3'-^{18}F-fluorothymidine PET (^{18}F-FLT). These two radiotracers reflect choline and thymidine metabolism and are related to cell proliferation [12, 13]. The obtained scaling exponents were $\beta = 1.21 \pm 0.08$ for gliomas and $\beta = 1.188 \pm 0.035$ for breast cancers (Fig. 1(c,f)), in agreement with a superlinear activity and providing support to the hypothesis of an increased glucose uptake to satisfy the proliferation demands.

Superlinear scaling laws have been found in varied scenar-

[1]Mathematical Oncology Laboratory, Universidad de Castilla-La Mancha, Spain; [2]Brain Metastasis Group, Spanish National Cancer Research Centre (CNIO), Madrid, Spain; [3]Neuro-oncology Unit, Health Institute Carlos III-UFIEC, Madrid, Spain; [4]Department of Physics, University of Tehran, Iran; [5]Department of Mathematics, Universidad de Cádiz, Spain; [6]Department of Radiation Oncology, Sanchinarro University Hospital, HM Hospitales, Spain; [7]Department of Neuroradiology, Sanchinarro University Hospital, HM Hospitales, Spain; [8] Inserm U1232, Centre de Recherche en Cancérologie et Immunologie Nantes-Angers, Nantes, F-44007, France; [9]Neurosurgery Clinic, Bern Insespital, Switzerland; [10]Radiology Unit, MD Anderson Cancer Center, Madrid, Spain; [11]Thoracic Surgery Unit, Hospital General Universitario de Albacete, Spain; [12]Nuclear Medicine Unit, Hospital General Universitario de Ciudad Real, Spain; [13]Fundación Instituto Valenciano de Oncología, Spain. *email: victor.perezgarcia@uclm.es

draft

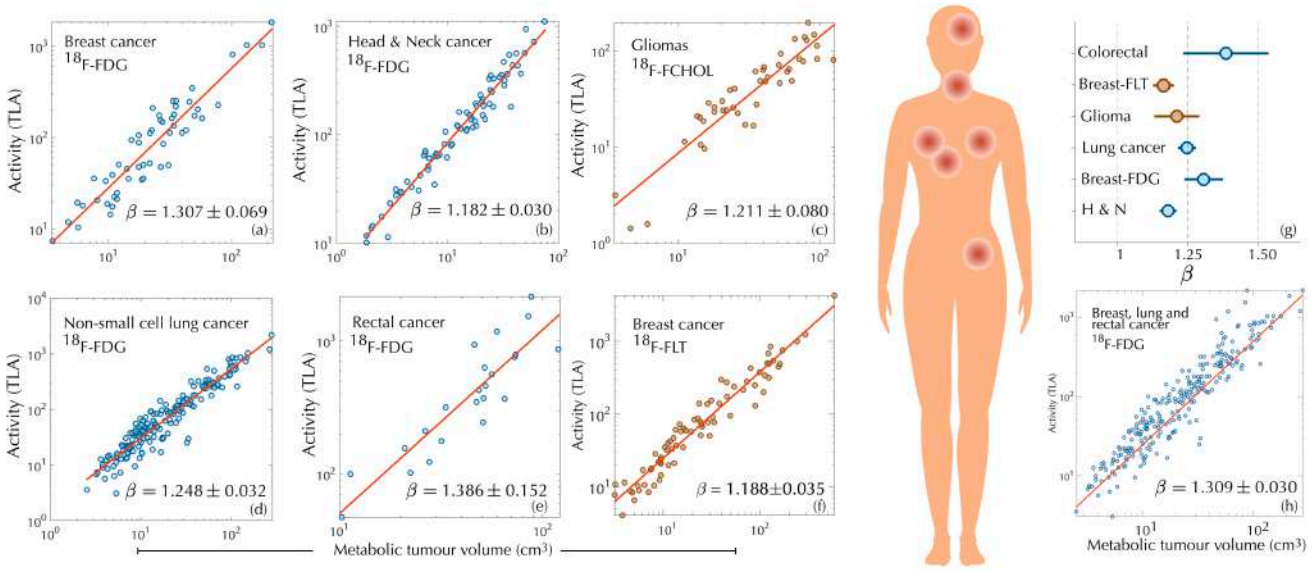

Figure 1 | A superlinear scaling law governs glucose uptake and proliferation in human cancers. Log-log plots of ^{18}F-FDG uptake (TLA) versus metabolic tumour volume on diagnostic PET for breast cancer, head & neck cancer, non-small-cell lung cancer and rectal cancer display superlinear ($\beta > 1$) allometric scaling laws. Diagnostic PET with proliferation radiotracers, either ^{18}F-FLT for breast cancer or ^{18}F-FCHOL for glioma, shows the same dependence pointing to the use of glucose mostly as a resource for biosynthesis. The fitted exponents cluster around $\beta = 5/4$. Joint records of patients imaged in the same institution with identical protocol (breast-FDG, lung and rectal cancers), show that a common scaling law governs the dynamics.

ios, ranging from urban infraestructures and socioeconomic networks to primitive life forms [2]. In contrast with sublinear scaling, which leads to stable bounded growth, superlinear scaling produces unbounded growth. For biological organisms, whole-body metabolic rates increase with size across prokaryotes, protists and metazoans, although each group is characterized by a distinctive scaling relationship that is unique to their body size range [14]. In heterotrophic prokaryotes the relationship between metabolic rate and body mass has an exponent $\beta > 1$, whereas for metazoans it is $\beta < 1$. Within an evolutionary perspective, the transition from simple prokaryotes to complex eukaryotes has shown not only a higher level of multicellular organization, but also a trend towards the 3/4 scaling exponent of Kleiber's law. Our results suggest that human cancers, as they progress, decrease the efficiency of their local vascular network [15], which would tend to increase their scaling exponents and significantly deviate from the 3/4 Kleiber's law.

To further quantify the relationship between tumour size and metabolism, let $B \propto V^{\beta}$ denote the metabolic rate of a tumour, where V is the volume occupied by viable cells. A simple mathematical model accounting for energy conservation describing the temporal dynamics of tumour growth is $B = aV + b\frac{dV}{dt}$, where the first and second terms correspond to cell maintenance and proliferation, respectively [16]. If most of the energy is used for cell biosynthesis, we may write

$$\frac{dV}{dt} = \alpha V^{\beta}. \qquad (1)$$

When $\beta > 1$, there is a finite time $t_{\rm crit} = t_0 + V_0^{1-\beta}/\left[\alpha(\beta-1)\right]$ at which the tumour 'blows up', where V_0 is the volume at time t_0 (see SI Section S1). Thus, the existence of a superlinear scaling law between proliferation and volume implies an increasingly accelerated volumetric growth and the formation of a singularity in a finite time. In real cancers such dynamics cannot be sustained to the blow-up point, since tumours are subject to physical and nutrient-supply constraints. In patients, such an accelerated growth in the final stages entails metabolic and spatial requirements incompatible with life.

There has long been discussion about the best mathematical model for describing tumour growth, most of them assuming different types of bounded dynamics [7, 17–20]. The data supporting these models comes from patient-derived cell lines cultured *in vitro* or, else, from either allotransplantation of murine cells into syngeneic immunocompetent inbred mice or from xenotransplantation of patient-derived cells into immunocompromised mice. These models have a number of shortcomings when compared with their human counterparts. They display loss of genetic heterogeneity and irreversible changes in gene expression due to long-term *in vitro* propagation [21] and exhibit a rapid non-autochthonous growth that results in a perturbed tissue architecture with alterations in the vascular, lymphatic and immune compartments.

To investigate whether explosive tumour growth could be observed in cancer patients, we looked for longitudinal imaging datasets of untreated tumours. Data of this type is scarce since growing tumours are typically either treated or -as in the case of palliative care patients- not followed up by imaging. Most available datasets had either incomplete information, no volumetric imaging and/or very few time points. Mandonnet and colleagues [22] studied the growth dynamics of untreated WHO grade II gliomas, Van Havenbergh [23] analysed petroclival meningiomas, and Heesterman et al [24] head and neck paragangliomas. Growth dynamics consistent with sublinear scalings were observed for those slowly growing tumours. To further confirm this idea, we collected longitudinal volumetric growth data from a set of lung hamartomas, the most frequent benign lung tumour type, and found a best fit of Eq. (1) with $\beta = 0.5 \pm 0.2$ (Fig. 2(d)). Hence, not all human tumours manifest an explosive growth.

We also collected imaging datasets of patients bearing tumours that were either malignant initially or became malignant over the course of the disease (see 'Methods' for a description of the patient datasets). The first one was a set of brain metastases in which one of the lesions was either below target definition or left without therapy due to medical reasons. A second set comprised initially WHO grade II gliomas that underwent surgery and then received no other treatment for long periods. The third was a set of patients enrolled in a lung cancer screening program. After detection of lung nodules with no signs of malignancy they where followed up by low-dose CT scans. Many of these tumours

Draft

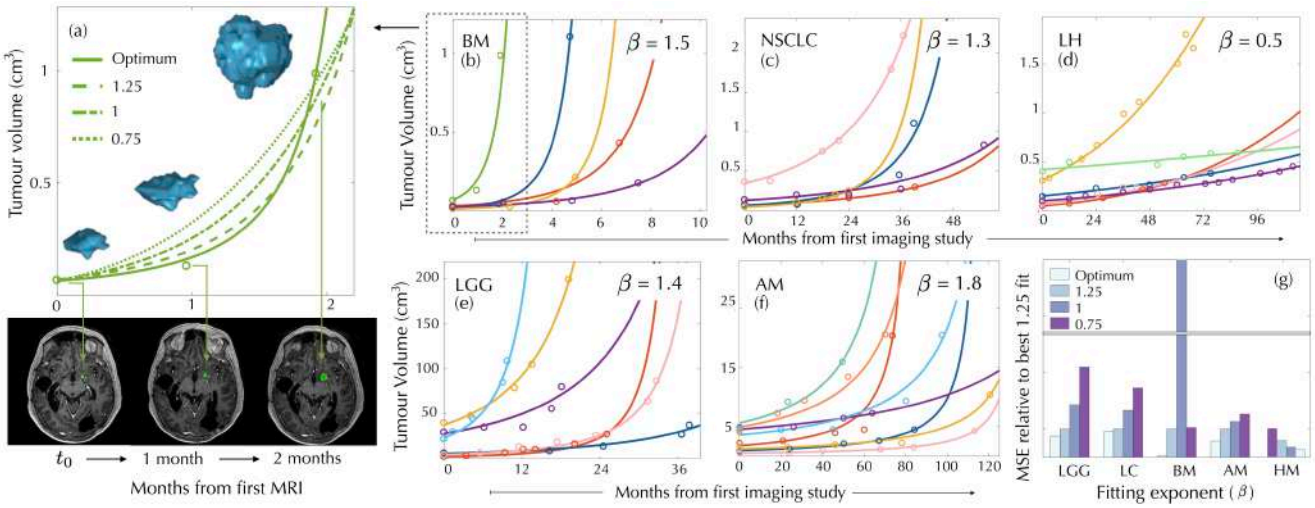

Figure 2 | Explosive longitudinal volumetric dynamics of untreated malignant human tumours. Longitudinal volumetric data for cancer patients with untreated brain metastases (BM), low grade gliomas (LGG), non-small-cell lung carcinomas (NSCLC), atypical meningiomas (AM) and lung hamartomas (LH). Solid curves show the fits with the optimal exponents (values provided in each subplot) giving the smallest mean square errors. The longitudinal 3D reconstruction of a BM and representative axial slices highlighting tumour location at three time points are displayed in the left panel together with the fitting curves obtained for different exponents. Mean square errors (MSE) for the five datasets and exponents 3/4, 1, 5/4 (taken as a reference) in comparison with the optimal exponent, are depicted in the lower right subplot.

accelerated their growth until a point at which further therapeutical actions were taken. Finally, we included a subset of petroclival meningiomas that showed signs of atypical behaviour (cases 5, 6, 9, 11 of Fig. 7 and cases 14, 18 of Fig. 8 in Ref. [23]). For each patient we fitted the longitudinal volumetric growth data using different power-law models expressed by Eq. (1). We tested the exponents $\beta = 3/4$ (size-limited Kleiber's law), $\beta = 1$ (exponential growth law) and then superlinear $\beta = 5/4$. Subsequently, we searched for the exponent that minimised the mean square error (MSE) for all patients within each tumour type. In all these examined cases, the existence of an explosive growth dynamics was confirmed [Fig. 2(b,c,e,f)]. A comparison of the MSEs for the different exponents and tumour types is shown in Fig. 2(g). We also performed a least-squares fitting of the α, β parameters for each patient and computed the mean and standard deviation for patients of each pathology. The results obtained were 1.493±0.0197 (BMs), 1.360±0.2922 (NSCLC), 1.466±0.269 (LGGs) and 1.690±0.452 (AMs) respectively. Thus, exponents obtained using the two methodologies were compatible between them and superlinear.

To determine whether animal models could also provide evidence of super-exponential tumour growth dynamics, we performed experiments on two animal models chosen because of their close relationship to their human counterparts. First, we injected the human lung adenocarcinoma brain tropic model H2030-BrM [25] into the heart of nude mice in order to induce the formation of brain metastasis from systemically disseminated cancer cells. The exponent best fitting the dynamics of the brain metastasis measured using bioluminiscence, assuming a dynamics ruled by Eq. (1), and data from all the mice was $\beta = 1.3$. The total tumour load in the animals showed similar behaviour, with $\beta = 1.25$ (Extended Data Fig. S1). In a second set of experiments, we injected primary glioma cells closely resembling the dynamics observed in patients [26] and expressing the luciferase reporter gene into the brains of nude mice. One month after the injection, weekly monitoring of the animals was started, measuring the total flow to assess tumour growth. The optimal exponents obtained were also $\beta = 1.25$.

Thus, a sustained increase in proliferation is supported both by the allometric scaling laws and the morphological longitudinal growth data during the tumour's natural history. We suspected that evolutionary dynamics could be the underlying process. Via genomic instability, driver gene mutations can confer, to subpopulations of clonal cells, somatic fitness advantages over other cells within the same tumour, and contribute to higher proliferation rates. Mutational events are expected to occur locally in space and time. However they require time to consolidate over the whole population [27], thus leading to an effective continuous change in the tumour's global proliferation rate. Phenotypic variability, manifested as trait fluctuations within identical genotypes, also leads to further selection of more proliferative cells [28].

The phenomenological model given by Eq. (1) lacks key hallmarks of real cancers. We explored *in silico* increasingly sophisticated spatio-temporal models incorporating cell migration and competition among different cell subpopulations. The first mathematical model that we put forward was a nonlocal Fisher-Kolmogorov equation (NLFK), encompassing random diffusive tumour cell motion and proliferation with saturation when reaching the local carrying capacity. The NLFK reads as

$$\frac{\partial u}{\partial t} = D\nabla^2 u + (\rho_0 + \rho_1 N(t))\left(1 - \frac{u}{K}\right)u, \qquad (2)$$

where $u = u(\mathbf{x}, t)$ denotes the tumour cell density, being a function of space $\mathbf{x}$ and time t. The model parameters are: the cell diffusion constant $D > 0$, the size-independent $\rho_0 > 0$ and size-dependent $\rho_1 \geq 0$ proliferation rates and K the local carrying capacity of the medium. The proliferation term in Eq. (2) includes a dependence on the total number of tumour cells $N(t) = \int u(\mathbf{x}, t)\, d^3\mathbf{x}$ on the grounds that, as total tumour size increases, there will be a higher probability of accumulated mutational events leading to more aggressive clones (see SI Section 2 for a derivation of the NLFK). The proliferation activity of the tumour, in the context of this model, is given by $M(t) = dN/dt$ and yields the scaling laws.

To quantify the role of spatial dimensionality d on the tumour growth scaling laws, we performed a mathematical analysis of Eq. (2) [see SI Section S2]. If $\rho_1 = 0$, one recovers the local FK equation for which the scaling exponent of $M(t)$ is $\beta = (d-1)/d < 1$, thus resulting in a sublinear growth. When $\rho_1 > 0$, the proliferation activity exhibits a superlinear scaling $\beta = 2 - 2/d$, leading to an explosive tumour growth only if $d = 3$. The tumour radial velocity,

Draft

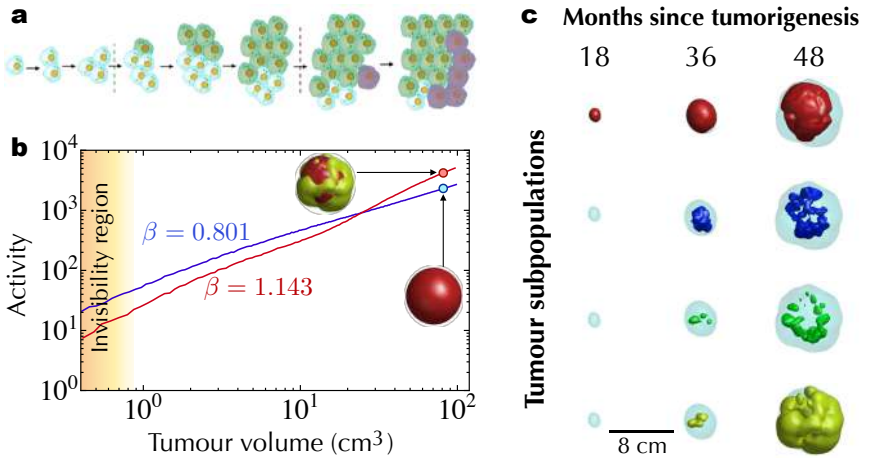

Figure 3 | Stochastic mesoscale models with evolutionary dynamics lead to superlinear scaling laws *in silico*. **a,** Schematic representation of the evolutionary dynamics included in the mesoscale tumour growth simulator model. Random time-local discrete events accounting for either mutations and/or phenotypic changes provide a competitive advantage to newly arising subpopulations. **b,** When a single tumour population is present, it grows continuously and displays a sublinear scaling law (blue line). In contrast, the evolutionary dynamics of a heterogeneous tumour (here consisting of four subpopulations, as set out in 'Methods') yielded superlinear growth dynamics (red line). **c,** Isosurfaces of four interacting cell subpopulations at different points in time showing the dynamics of dominance by the most aggressive cells (higher indices correspond to more aggressive clones as described by the model parameters).

which is a relevant metric in the clinic, can also be obtained in closed form as $v_d(t) = M(t)/C_d N^{(d-1)/d}(t)$, where $C_1 = 2$ (1D), $C_2 = (4\pi)^{1/2}$ (2D), and $C_3 = (36\pi)^{1/3}$ (3D). Hence, dimensionality plays an essential role in the emergence of superlinear allometric laws within the NLFK model Eq. (2).

To further elucidate the contribution of different interacting cell subpopulations to the global tumour dynamics, we developed a stochastic mesoscale tumour growth simulator enabling cells to undergo replication, apoptosis, migration to neighbouring voxels and genotypic/phenotypic transitions (see 'Methods' and SI Section S3). By mesoscale we refer to a coarse-grained approach that can reach computationally clinically relevant tumour sizes ($\sim 10^2$ cm^3) by working at the population level rather than on individual cells. Extensive *in silico* simulations showed superlinear scaling in broad regions of the parameter space, matching both the volume range and time kinetics observed in patients (Fig. 3). Superlinear behaviour was present in so far as there was a persistent overtaking of cell subpopulations by more aggressive ones. The dynamics of uniform populations, without *in silico* evolutionary dynamics, displayed sublinear scalings (Fig. 3). Other mathematical models incorporating short-range dispersal and cell turnover have reported changes in spatial growth due to the underlying evolutionary dynamics [29, 30].

Scaling laws are very intriguing properties of physical and biological systems that shed light on their dynamics. They have a fundamental value but are often of limited applicability. We hypothesized that, once a scaling law of the form $Z = \alpha V^{\beta}$ is set as a reference for a specific cancer type, those with radiotracer uptake higher than the reference level, as defined by the scaling law, could be more aggressive than those with lower activity. Thus, we computed the distance with respect to a reference scaling law (DSL) for each tumour j and dataset for which survival information was available, via $\mathrm{DSL}_j = \mathrm{TLA}_j - \alpha \mathrm{MTV}_j^{\beta}$, and compared two sets with different DSL for the whole range of values of the prefactor α, as described in Methods. Figure 4 summarizes our results for a fixed exponent $\beta = 5/4$ in four patient cohorts with distinct cancer types. We found ranges of threshold values classifying patient subpopulations into DSL groups with survival differences as measured by the Harrell's c-index.

The classical metabolic variables MTV and TLA classified gliomas (MTV: c-index = 1.0, $p = 0.013$; same for TLA) and breast cancer patients (MTV: c-index = 0.824, $p = 0.098$; TLA: c-index = 0.87, $p = 0.01$) but neither lung cancer nor head and neck patients. Hence, the superlinear metabolic scaling laws provided prognostic metrics that were more robust than other classical PET-based indices.

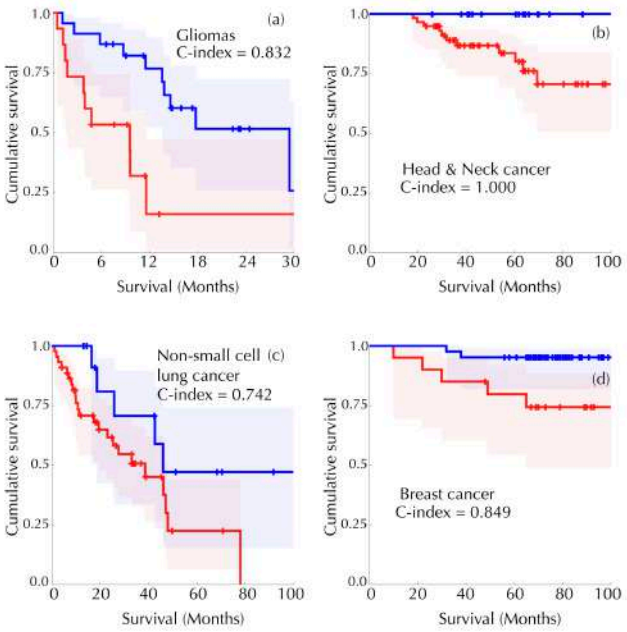

Figure 4 | Scaling laws allow for cancer patient classification into prognostic groups. Patient tumours were classified as hyperactive (TLA $> \alpha V^{5/4}$; DSL > 0) or hypoactive (TLA $< \alpha V^{5/4}$; DSL < 0) using the metabolic scaling law as a reference. Survival differences between groups were compared using Kaplan-Meier analysis and the c-index. Shown are Kaplan-Meier survival curves and the best c-index values obtained for: (a) Gliomas (p =0.001, c-index = 0.832, α = -0.24867). (b) Head and Neck cancer (p =0.05, c-index = 1.0, α = -0.0041776). (c) Stage III and IV resectable lung cancer patients (p=0.09, c-index = 0.742, α = -0.40334). (d) Breast cancer (p =0.019, c-index = 0.849, α =-0.65034).

The observation of superlinear metabolic scaling laws and explosive behaviour of malignant tumours opens up many avenues of research. Our stochastic mesoscopic framework showed how evolutionary dynamics leads to superlinearity through the competition and consolidation of different tu-

mour subpopulations. However, evolutionary steps could be based on mutations or phenotypic variability. When an initial driver mutation appears locally in space, even when it is more advantageous, it requires some time to consolidate. During this time window our simulations showed a continuous acceleration due to the fact that an increasing number of cells bear this new genotype. However, once this mutation is consolidated, a plateau could develop, provided no new driver mutations have appeared in the meantime. For our choice of parameters the effective dynamics resulting from our discrete simulations was in general superlinear, in agreement with our observations based on patient and animal experimental data.

The specific mechanisms leading to an increase in the proliferation with the tumor physical size could differ between types of cancers. Some of them could be of evolutionary nature related to genotype or phenotype changes as discussed before, involve the random selection of higher fitness values [31], as well as to the possibility of acquiring drivers before deleterious passengers [32], etc. Other potentially relevant processes arise in the interplay of glycolysis and tumour vascularization and oxygenation, such as the onset of the Warburg effect induced by hypoxic episodes. Others could be related to changes in the interaction between the tumour and the surrounding tissue, the action of the immune system, alterations in the tumour microenvironment such as acidosis [33]. Some of these effects, while possibly driven by mutational alterations, may in fact be ecological in nature. It is interesting to point out that small tumors below the spatial scale studied here, may have superlinear behaviour due to different reasons: Allee effect models in ecology have decreased growth rates at smaller tumor sizes, and these produce growth curves that are potentially indistinguishable from superlinear growth laws when fitting a few points from data. Other size-related effects for small tumors may involve the interaction with the immune system: small tumors may struggle to outgrow the immune system at first, but once they creep up to a large enough size, the immune death would become negligible.

Our results emphasise the need to gain a better understanding of the evolutionary steps in different tumour histologies and to target these transformations to avoid growth acceleration. They also raise the question of whether working with experimental tumour models that show slower than superexponential growth could miss essential features of cancer dynamics. Finally, the role played by allometric scaling laws in human cancers under different therapies and the ultimate development of resistances has not yet been explored.

In summary, we have found superlinear metabolic scaling laws in human cancers. These laws differ substantially from the Kleiber's law governing many life forms, and point to accelerated growth due to underlying evolutionary dynamics selecting more aggressive subpopulations. Longitudinal volumetric data from malignant tumours shows explosive growth beyond classical growth-limited or exponential laws. Our mathematical models, assuming intrinsic evolutionary dynamics, put forward a mechanistic explanation for the observed phenomenology and predict that the emergence of superlinear scaling laws is an inherently three-dimensional phenomenon. We hope this study will stimulate further activity in the field of allometric scaling laws in cancer.

References

1. Kleiber, M. Body size and metabolism. *Hilgardia* **6,** 315-351 (1932).
2. West, G. *Scale: The Universal Laws of Growth Innovation, Sustainability, and the Pace of Life in Organisms, Cities, Economies and Companies* (Penguin Press, New York, 2017).
3. West, G. B., Brown, J. H. & Enquist, B. J. A general model for the origin of allometric scaling laws in biology. *Science* **276,** 122-126 (1997).
4. Savage, V. M. et al. The predominance of quarter-power scaling in biology. *Funct. Ecol.* **18,** 257-282 (2004).
5. Reich, P. B., Tjoelker, M. G., Machado, J. L. & Oleksyn, J. Universal scaling of respiratory metabolism, size and nitrogen in plants. *Nature* **439,** 457-461 (2006).
6. Enquist, B. J. et al. Biological scaling: does the exception prove the rule? *Nature.* **445,** E9-10 (2007).
7. Guiot, C., Degiorgis, P. G., Delsanto, P. P., Gabriele, P. & Deisboeck, T. S. Does tumour growth follow a universal law? *J. Theor. Biol.* **225,** 147-151 (2003).
8. Herman, A. B., Savage, V. M. & West, G. B. A quantitative theory of solid tumor growth, metabolic rate and vascularization. *PLoS One* **6,** e22973 (2011).
9. Milotti, E., Vyshemirsky, V., Sega, M., Stella, S. & Chignola, R. Metabolic scaling in solid tumours. *Sci. Rep.* **3,** 1938 (2013).
10. Palm, W. & Thompson, C. B. Nutrient acquisition strategies in mammalian cells. *Nature* **546,** 234-242 (2017).
11. Zhu, J. & Thompson, C. B. Metabolic regulation of cell growth and proliferation. *Nat. Rev. Mol. Cell Biol.* **20,** 436-450 (2019).
12. De Grado, T. R., Reiman, R. E., Price, D. T., Wang, S. & Coleman, R. E. Pharmacokinetics and radiation dosimetry of ^{18}F-fluorocholine. *J. Nucl. Med.*, **43,** 92-96 (2002).
13. Barwick, T., Bencherif, B., Mountz, J. M. & Avril, N. Molecular PET and PET/CT imaging of tumour cell proliferation using F-18 fluoro-L-thymidine: a comprehensive evaluation. *Nucl. Med. Commun.*, **30,** 908-917 (2009).
14. DeLong, J. P., Okie, J. G., Moses, M. E., Sibly, R. M. & Brown, J. H. Shifts in metabolic scaling, production, and efficiency across major evolutionary transitions of life. *Proc. Natl Acad. Sci. USA* **107,** 12941-12945 (2010).
15. De Palma, M., Biziato, D. & Petrova, T. Microenvironmental regulation of tumour angiogenesis. *Nat. Rev. Cancer* **17,** 457-474 (2017).
16. West, G. B., Brown, J. H. & Enquist, B. J. A general model for ontogenetic growth. *Nature* **413,** 628-631 (2001).
17. Gerlee, P. The model muddle: in search of tumor growth laws. *Cancer Res.* **73,** 2407-2411 (2013).
18. Rodriguez-Brenes, I. A., Komarova, N. L. & Wodarz, D. Tumor growth dynamics: insights into evolutionary processes. *Trends Ecol. Evol.* **28,** 597-604 (2013).
19. Benzekry, S. et al. Classical mathematical models for description and prediction of experimental tumour growth. *PLoS Comput. Biol.* **10,** e1003800 (2014).
20. Talkington, A. & Durret, R. Estimating tumour growth rates in vivo. *Bull. Math. Biol.* **77,** 1934-1954 (2015).
21. Gengenbacher, N., Singhal, M. & Augustin, H. G. Preclinical mouse solid tumour models: status quo, challenges and perspectives. *Nat. Rev. Cancer* **17,** 751-765 (2017).
22. Mandonnet, E. et al. Continuous growth of mean tumour diameter in a subset of grade II gliomas. *Ann. Neurol.* **53,** 524-528 (2003).
23. Van Havenbergh, T., Carvalho, G., Tatagiba, M., Plets, C. & Samii, M. Natural history of petroclival meningiomas. *Neurosurgery* **52,** 55-64 (2003).
24. Heesterman, B. L. et al. Mathematical models for tumour growth and the reduction of overtreatment. *J. Neurol. Surg. B* **80,** 72-78 (2019).
25. Nguyen, D.X. et al. WNT/TCF signaling through LEF1 and HOXB9 mediates lung adenocarcinoma metastasis. *Cell* **138,** 51-62 (2009).
26. Gargini, R. et al. The IDH-TAU-EGFR triad defines the neovascular landscape of diffuse gliomas. *Sci. Trasl. Med.* (to appear) (2020).
27. Hallastschek, O. & Fisher, D. S. Acceleration of evolutionary spread by long-range dispersal. *Proc. Natl Acad. Sci. USA* **111,** E4911-E4919 (2014).
28. Deforet, M., Carmona-Fontaine, C., Korolev, K. S. & Xavier, J. B. Evolution at the edge of expanding populations. *Am. Nat.* **194,** 291-305 (2019).

Preprint

29. Waclaw, B., Bozic, I., Pittman, M. E., Hruban, R. H., Vogelstein, B. & Nowak, M. A. A spatial model predicts that dispersal and cell turnover limit intratumour heterogeneity. Nature **525,** 261-264 (2015).
30. Komarova, N. L. Spatial interactions and cooperation can change the speed of evolution of complex phenotypes. *Proc. Natl Acad. Sci. USA* **111,** 10789-10795 (2014).
31. Durrett, R., Foo, J., Leder, K., Mayberry, J. & Michor, F. Evolutionary dynamics of tumor progression with random fitness values. *Theor. Popul. Biol.* **78,** 54-66 (2010).
32. McFarland, C. D., Mirny, L. A., Korolev, K. S. Tug-of-war between driver and passenger mutations in cancer and other adaptive processes. *Proc. Natl Acad. Sci. USA* **111,** 15138-15143 (2014).
33. Robertson-Tessi, M., Gillies, R. J., Gatenby, R. A., Anderson, A. R. Impact of metabolic heterogeneity on tumor growth, invasion, and treatment outcomes. *Cancer Res.* **75,** 1567-1579 (2015).

Acknowledgements.
This research has been supported by the James S. Mc. Donnell Foundation 21st Century Science Initiative in Mathematical and Complex Systems Approaches for Brain Cancer (Collaborative awards 220020560 and 220020450), Ministerio de Economía y Competitividad/FEDER, Spain (grant number MTM2015-71200-R), Junta de Comunidades de Castilla-La Mancha (grant number SBPLY/17/180501/000154).

Author contributions
V.M.P.-G. designed the research, collected and processed data, performed the fittings, developed and simulated the mathematical models. J.J.B. collected data, processed data, performed fitting tasks and developed the automatic segmentation algorithm. J.P.-B. collected and processed data. O.L.-T. collected and processed data and fitted the longitudinal volumetric data. M.V., L.X, P.G.-G., P.S.-G., E.H., R.H., performed the experiments in animal models. E.A., P.S., M.M., D.A., A.A.-R., A.F.H-M collected data. G.J. collected and processed data. M.P.-C. processed data. G.F.C., J.J.B., J.B.-B., Y.A. and A.M. developed and simulated the mathematical models. A.M.G.-V., designed the research, collected and processed data. V.M.P.-G. and G.F.C. drafted the manuscript. All authors edited and approved the final manuscript.

Competing interests
The authors declare no competing interests.

Ethical approval
We have complied with all relevant ethical regulations. Human data were obtained either from public repositories (TCIA) or in the framework of several retrospective or prospective observational clinical studies approved by the corresponding institutional review boards (for details see Methods). Animal care and experimental procedures were performed in accordance to the European Union and National guidelines for the use of animals in research and were reviewed and approved by the Research Ethics and Animal Wellfare Committee at Instituto de Salud Carlos III de Madrid (PROEX 244/14) (glioma cells) and in accordance with a protocol approved by the CNIO, Instituto de Salud Carlos III and Comunidad de Madrid Institutional Animal Care and Use Committee (H2030-BrM3 cells).

Additional information
Supplementary information is available for this paper.

Correspondence and requests for materials should be addressed to V.M. Pérez-García (`victor.perezgarcia@uclm.es`).

draft

Methods

Patients and image acquisition. Several patient datasets were included in our study. Patient subgroups 1-6 were used for the construction of the scaling laws (1,2,4,5 also for the survival studies). Patient subgroups 7-10 were used for the study of the longitudinal tumour volumetric dynamics. Overall survival (OS) was determined as the time from pretreatment imaging to death or last follow-up.

Breast Cancer Patients (subgroup 1). All reported patients were participants of a multicenter prospective study started in September 2009. The study was approved by the Institutional Review Board (IRB), and written informed consent was obtained from all patients. The inclusion criteria were the following: (1) newly diagnosed locally advanced breast cancer with clinical indication of neoadjuvant chemotherapy (NC), (2) lesion uptake higher than background, (3) absence of distant metastases confirmed by other methods previous to the request of the PET/CT for staging, and (4) breast lesion size of at least 2 cm. 54 patients (100% women, age rank 25-80, median 50 years) were included in this dataset. Of them 18% were lobular carcinoma and 82% ductal carcinomas. The TNM data were: 54% T2, 18% T3, 28% T4; 28% N0, 55% N1, 6% N2, 11 % N3; 100% M0.

PET/CT examinations were performed on the same dedicated whole-body PET/CT scanner (Discovery DSTE-16s, GE Medical Systems) in three-dimensional (3D) mode. The acquisition began 60 minutes after intravenous administration of approximately 370 MBq (10 mCi) of ^{18}F-FDG and was performed following a standardized protocol. The image voxel size was 5.47 mm × 5.47 mm × 3.27 mm, with a slice thickness of 3.27 mm and no gap between slices. Matrix size was 128 × 128.

Head & Neck cancer patients (subgroup 2). These patients were obtained from the The Cancer Imaging Archive (TCIA) [34] Head-Neck-PET-CT collection (H& N1 data set) [35]. This cohort was composed of 92 patients with primary squamous cell carcinoma of the head-and-neck (stages I-IV) treated between 2006 and 2014 at Hopital General Juif, Montreal, QC. 76 consecutive patients from this subset satisfying the inclusion criteria (availability of pretreatment PET studies, presence of a well-defined primary tumour and lesion size larger than 2.0 cm) were included in our study. Data for the cohort were: age rank 18-84, median 62 years; 63 male, 13 female; 13 cancers of larynx, 3 hypopharynx, 11 nasopharynx, 49 oropharynx. Staging data are 3 stage II, 1 stage IIB, 26 stage III, 44 stage IVA, 2 stage IVB. Finally, the TNM information is 11 T1, 19 T2, 34 T3, 12 T4; 11 N0, 16 N1, 7 N2a, 27 N2b, 13 N2c, 2 N3; 72 M0, 4 Mx.

Eligible patients had FDG-PET scans obtained on a hybrid PET/CT scanner (Discovery ST, GE Healthcare) within 37 days before treatment (median: 14 days). A median of 584 MBq (range: 368-715) was injected intravenously. Imaging acquisition of the head and neck was performed using multiple bed positions with a median of 300 s (range: 180-420) per bed position. The slice thickness resolution was 3.27 mm for all patients and the median in-plane resolution was 3.52 × 3.52 mm^2 (range: 3.52-4.69).

Rectal cancer (subgroup 3). A retrospective observational study (SCALAWS: Scaling laws, shape factors and fractal measures in human cancers) was designed and approved by the IRB of the participating institutions. Inclusion criteria were: histological confirmation of advanced rectal cancer diagnosis, availability of pretreatment PET/CT and lesion size larger than 2 cm. A total of 23 rectal cancer patients (16 male, 7 female, age rank 54-80, median age 72 years) from the period October 2007 to October 2009 were included in the study. PET/CT examinations were performed on the same dedicated whole-body PET/CT scanner (Discovery DSTE-16s, GE Medical Systems) in three-dimensional (3D) mode. The acquisition began 60 minutes after intravenous administration of approximately 370 MBq (10 mCi) of ^{18}F-FDG and was performed following a standardized protocol.

Lung cancer (subgroup 4). 175 patients (153 men, 22 women, age rank 41-84, median 65 years) were included in the SCALAWS study from a dataset of lung cancer patients that received surgery in the period June 2007 to December 2016. Histologies were 63 squamous cell carcinoma and 112 adenocarcinoma. Staging information was: 69 stage I, 70 stage II, 33 stage III, 3 stage IV. The N staging was 107 patients N0, 46 N1 and 22 N2. All patients had M0. PET protocol and machine were as in subgroup 1. We set the inclusion criterion that minimal lesion size should be larger than 2.0 cm.

Gliomas (subgroup 5). A prospective multicenter and non-randomized study was designed (FuMeGA: Functional and Metabolic Glioma Analysis), and approved by the IRB of the participanting institutions. Informed consent was obtained from all patients. Patients were included consecutively. A basal ^{18}F-fluorocholine PET/CT was performed in patients suspicious of glioma after magnetic resonance imaging (MRI) with an operable brain lesion and a good performance status (ECOG≤2). For the present analysis, only patients with pathologically confirmed brain glioma, and unifocal lesions of size larger than 2.0 cm were included. Our study included 44 patients from the period 2017-2019 (15 women, 29 men), age rank 23-79, median 60 years. Histologies were 32 glioblastoma IDH1wt, three glioblastoma IDH1mut, two oligodendroglioma, four difuse astrocytoma and three anaplastic astrocytoma.

PET/CT scans were performed in the same hybrid equipment (Discovery DSTXL-1, General Electric). PET adquisition was initiated 40 min after the intravenous administration of 185 MBq of ^{18}F-Fluorocholine. First, a brain scan was performed starting with a low-dose CT transmission study (modulated 120 kV and 80 mA) without intravenous contrast followed by a tridimensional (3D) emission study with an acquisition time of 20 min (one single bed), voxel size of 2.3 × 2.3 × 3.3 mm in a matrix of 128 × 128 and reconstructed using the CT images for attenuation correction and applying an iterative reconstruction algorithm.

Breast cancer patients (subgroup 6). Pretreatment ^{18}F-FLT PET/CT scans of patients of the American College of Radiology Imaging Network (ACRIN) 6688 observational, nonrandomized, multicenter phase II study available in the TCIA (ACRIN-FLT-Breast) were included in the study [36]. This dataset included histologically confirmed breast cancer patients (100% women), of them 46.8% premenopausal and 52.2% postmenopausal. TNM were 3% TX, 1% T1, 47% T2, 34% T3 and 14% T4; 3% NX, 29% N0, 51% N1, 11% N2, 6% N3; and 100% N0.

Inclusion criteria were: (1) primary breast cancer measuring 2.0 cm or more, (2) being a candidate for neo-adjuvant chemotherapy and surgical resection of residual primary tumour after chemotherapy, and (3) no evidence of stage IV disease. All patients received a baseline pretreatment ^{18}F-FLT PET/CT study within 4 weeks before NAC initiation. After the injection of 2.6 MBq/kg (mean, 167 MBq; range, 110-204 MBq), a whole-body image (5-7 bed positions) was obtained at 60 min (mean, 70 min; range, 50-101 min). All patients were scanned on calibrated and ACRIN- accredited PET/CT scanners, which included review of image quality and testing of SUVs using a uniform phantom and review of images. 75 patients were included in the study (100% female, age rank 22-83 y, median 50 y).

Brain metastasis patients (subgroup 7). Patients included were participants in the study METMATH (Metastasis

CLOSED

and mathematics), a retrospective multicenter and non-randomized study approved by the IRB of the participanting institutions. We reviewed the METMATH records to look for patients satisfying the following inclusion criteria: patients diagnosed of brain metastasis of a primary lung cancer with an untreated lesion with three or more consecutive MRI studies before treatment. Five patients satisfied the inclusion criteria. Patients data were: four women, one man; age rank 38-67, median 52 years. Primaries were four non-small cell lung cancer and one breast luminal b cancer. For these patients only the dynamics of the brain metastases were analyzed. A total of 16 imaging studies were included, the rank of studies per patient being 3-4.

Postcontrast T1-weighted sequence was gradient echo using 3D spoiled-gradient recalled echo or 3D fast-field echo after intravenous administration of a single-dose of gadobenate dimeglumine (0.10 mmol/kg) with a (6-8)-min delay.

All MRI studies were performed in the axial plane with either a 1.5 T Siemens scanner, a 3 T Philips scanner and a 1 T Philips scanner. Imaging parameters were no gap, slice thickness of 1 - 1.6 mm, 0.438-0.575 mm xy resolutions, and 0.8 - 1.3 mm spacing between slices.

Lung cancer patients (subgroup 8). Patients included were participants in the study SCALAMATH. Five patients (3 men, 2 women) were included. Three of them were diagnosed as adenocarcinoma and two as squamous cell carcinomas. Age rank was 60-72 years (median 68). All of them were initially stage I tumours and progressed without treatment.

We drew from the database of follow-up screenings in I-ELCAP between 2008 and 2019, which were performed according to a common protocol [37] using low-dose CT (LDCT). Enrollment was limited to those aged 50 years or older, with a smoking history of at least 10 pack-years, no previous cancer and general good health. Participants harboring parenchymal solid or part-solid non calcified nodule with at least three or more follow-up CTs were identified according to specified criteria in the protocol. A total of 22 imaging studies were used, the rank of studies per patient being 3 to 6 (mean 4).

Thoracic CT scans used a 16 acquisition channels mutidetector computed tomography (Siemens Emotion 16, Erlangen, Germany) with maximum section collimation of 1 mm, 0.7 mm of spacing between slices, 1 mm of slice thickness and a range of xy resolution of 0.584 - 0.783 mm. The CT scans were done at 120 kVps y 30 mAs, and less than 1 s tube rotation time. Contiguous images were reconstructed in the trans-axial plane using 1 mm thickness. Lung image sets were reconstructed with a high frequency algorithm and mediastinal image sets were reconstructed with an intermediate frequency algorithm.

Lung cancer diagnosis was made by histopathological examination of needle core biopsy or resection specimens, or by cytopathological examination of bronchoscopic or needle aspiration biopsy samples. Resected tumours were classified using the WHO classification of lung neoplasms. Adenocarcinomas were classified according to the International Association for the Study of Lung Cancer American Thoracic Society European Respiratory Society classification of lung adenocarcinoma. All lung cancer diagnoses were centrally reviewed. The tumours were staged using the International Association for the Study of Lung Cancer Staging Guidelines [37].

Low-grade glioma patients (subgroup 9). 82 patients diagnosed of grade II gliomas (biopsy/surgery confirmed astrocytoma, oligoastrocytoma or oligodendroglioma according to the WHO 2007 classification) and followed at the Bern University Hospital between 1990 and 2013 were initially included in the study. The study was approved by Kantonale Ethikkommission Bern (Bern, Switzerland), with approval number: 07.09.72.

Of that patient population, we selected patients receiving either no treatment or only surgery for which at least five post-surgery consecutive images showing tumour growth were available. Six patients satisfied our inclusion criteria. Patients data were: age rank 29-50, mean 37 years. All of them were initially diagnosed as grade II gliomas (four astrocytomas and two oligodendrogliomas). A total of 34 imaging studies were used, the rank of studies per patient being 4 to 7 (mean 6).

Lung hamartoma patients (subgroup 10). Six patients (five men, one woman; age rank 51-63, median 58 years) diagnosed of lung hamartomas participants of the protocol SCALAMATH with longitudinal follow-up were included in the study. Imaging methods were the same as in subgroup 8. A total of 46 imaging studies were used, the rank of studies per patient being 5 to 12 (mean 8).

PET image analysis (patient subgroups 1-6). At least an experienced nuclear medicine physician and an imaging engineer independently assessed the PET scans in an Advantage Windows station (v.4.). In case of discordance a third evaluator revised the images. In the visual evaluation, a PET scan was considered as positive if any uptake, higher than normal tissue background, was detected. Only positive PET scans were considered for tumour segmentation, i.e. those having a SUVmax larger than twice the background activity readings.

PET images in DICOM (Digital Imaging and Communication in Medicine) files were imported into the scientific software package Matlab (R2018b, The MathWorks, Inc., Natick, MA, USA). The tumour PET images were first manually placed in a 3D box and then semi-automatically delineated using a grey-level threshold chosen to identify the metabolic tumour volume. Then, segmentations were corrected manually slice by slice. An in-house software was developed under Matlab software based on its image processing toolboxes, allowing the segmentations to be corrected on a tablet using a digital pencil.

All segmentations were performed by at least a nuclear medicine physician and an imaging engineer, both with more than 5 years of experience in tumour segmentation. In many cases one or two additional segmentations by imaging engineers were performed to verify the robustness of the methodology and to obtain consensus segmentations. Physiological activity contiguous with tumour uptake, as e.g. choroid plexus or skull in the brain, was manually excluded from the tumour segmentations. To avoid observer dependent biases, for those tumour histologies well separated from surrounding structures with physiological uptake an automatic segmentation algorithm was developed (see next subsection).

The radiotracer standardized uptake values (SUV) were computed for each voxel using the formula

$$\mathrm{SUV} = \frac{S_v \times R_S \times W}{R_{TD} \times D_F \times e^{\ln(2) E_t / H_F}}. \qquad (3)$$

Where S_v is the stored value, R_S the rescaled slope, W is the patient weight, R_{TD} is the radiopharmaceutical injected dose and H_F its half-life, D_F is the decay factor, and E_t is the elapsed time for each slice processed.

Global metabolic parameters were obtained, specifically the metabolic tumour volume (MTV, the volume of the VOI after segmentation) and the total lesion activity (TLA, the sum of all local SUV values over the VOI). Also relevant local metrics such as the maximum value of the SUV over the segmented lesion was stored (SUVmax). Since radiotracer uptake is very low in necrotic areas, they typically do not contribute to TLA and MTV.

Automatic Segmentation algorithm for PET images. An automatic segmentation algorithm was designed and implemented in Matlab to carry out the segmentations of tumours in patient subgroups 1, 4, and 6.

Draft

Each PET image contains a spatial map of the SUV activity ($u(\vec{x})$). Each SUV threshold defines an isosurface in the function u. This means that the isosurfaces are parametrized by the threshold values (u_*) and all of the threshold-based potential segmentations of the bulk tumour are indeed isosurfaces of $u(\vec{x})$. The contour that better delineates the tumour is the one that maximizes the contrast in the image over the adjacent isosurfaces. To quantify this, we used the functional

$$\mathcal{F}(u_*;\lambda) = (1-\lambda u_*)\int_{\{\vec{x}/u(\vec{x})=u_*\}} |\nabla u|^2\, dS, \qquad (4)$$

that was computed for each image and each possible threshold value u_*. The surface integral of the squared gradient quantifies the variation in SUV over the isosurface of SUV level u_*. The factor $(1-\lambda u_*)$ was chosen to penalize higher SUV values in order to get a more accurate delineated zone. For each image, the functional (4) was computed for every possible threshold value u_* from the maximum SUV in the image. The value u_* that maximizes (4) was then selected as segmentation threshold and, therefore, the corresponding isosurface used as bulk segmentation. This is an example of variational, gradient based segmentations that have been used in the literature of PET segmentation such as the method of snakes [39, 40], although in three-dimensional scenarios and restricting the contours to isosurfaces.

The value of the parameter $\lambda = 0.26$ was selected by performing an optimization process where a set of breast and lung tumour segmentations performed by a board of three imaging engineers were used as ground truths and compared to those provided by variable values of λ. Note that the case $\lambda = 0$ corresponds to the choice of the tumor areas with stronger gradients and allows for the segmentation of the tumor core, excluding the lower densities halos surrounding the higher SUV values tumor regions.

For the application of the method, a point belonging to the tumour has to be chosen initially. While the isosurface of a given value might be extensive along the domain, only the part enclosing the initial point are taken into account for the calculations. After having selected the points the SUV range for the image is divided in 512 equally distributed partitions which constitute a discretization for the possible threshold points u_*. The functional (4) is then applied using descending values for u_* starting from SUVmax. The process is continued until a local maximum for $\mathcal{F}(u_*;\lambda)$ is found. When this maximum is followed by a concatenation of five points with a strictly descending tendency the algorithm stops and the u_* that maximizes the functional is used as threshold value.

MRI image analysis (patient subgroups 7 & 9). Brain metastasis T1-weigthed images were collected in DICOM format and analysed by the same image expert (OLT, 2 years of expertise on tumour segmentation). The methodology was the same as described for patient subgroups 1-6. After the segmentations an experienced radiologist (EA) revised and validated the tumour delineation.

For the study of patients in subgroup 9, T2/FLAIR MRI studies were used to define the tumour volume. Radiological glioma growth was quantified by manual measurements of tumour diameters on successive MRI studies (T2/FLAIR sequences). Since some of the older patients were available only as jpeg images we computed the volume using the ellipsoidal approximation. The three largest tumour diameters (D_1,D_2,D_3) along the axial, coronal and sagittal planes were measured and tumour volumes estimated using the equation $V = (D_1 \cdot D_2 \cdot D_3)/2$, following the standard practice [41].

CT image analysis (patient subgroup 8, 10). Patients included were participants in the study SCALAMATH. CT images of lung cancer nodules were obtained in DICOM format. An experienced radiologist (EA) localized the lesion and then an image expert (OLT) performed the segmentations following the same methodology as with subgroups 1-7.

Glioma cells. Primary glioma cells (L0627) were kindly provided by Rosella Galli (San Raffaele Scientific Institute, Milan, Italy) and were grown in complete medium: Neurobasal (Fisher) supplemented with B27 (1:50) (Fisher); Glutamax (1:100) (Fisher); Penicillin-streptomycin (1:100) (Lonza); 0.4 % heparin (Sigma-Aldrich); 40 ng/ml EGF and 20 ng/ml bFGF2 (Peprotech). Cells were passaged after enzymatic disaggregation using Accumax (Milipore). In order to monitor tumour growth, cells were infected with lentiviral particles expressing Fluc (pLV-Hygro-EF1A-Luciferase) (Vector-Builder) and selected in the presence of Hygromycin.

Mouse glioma xenografts. We injected primary glioma cells expressing the luciferase reporter gene into the brain of nude mice. One month after the injection, we started monitoring the animals weekly using IVIS Spectrum In vivo Imaging System. The Total Flux (in photons per second) was measured to assess tumour growth. Animal care and experimental procedures were performed in accordance to the European Union and National guidelines for the use of animals in research and were reviewed and approved by the Research Ethics and Animal Welfare Committee at our institution (Instituto de Salud Carlos III, Madrid) (PROEX 244/14). Stereotactically guided intracranial injections in athymic nude Foxn1nu mice were performed by administering 1×105 L0627 cells resuspended in 2 μl of culture media. The injections were made into the striatum (coordinates: A-P, ±0.5 mm; M-L, +2 mm; D-V, -3 mm; related to Bregma) using a Hamilton syringe. One month after the injection we started monitoring the reporter expression in the tumours. For that, animals received and intraperitoneal injection of Luciferin (Fisher) (150mg/Kg) and the Luciferase activity was visualized in an IVIS Spectrum in vivo imaging system (Perkin Elmer).

Animal studies with H2030-BrM3 cells. The human lung adenocarcinoma brain tropic model H2030-BrM [25] was injected into the heart of nude mice in order to induce the formation of brain metastasis from systemically disseminated cancer cells. Brain colonization and growth of metastases were followed using non-invasive bioluminescence imaging since BrM cells express luciferase. Upon administration of the substrate D-luciferin, bioluminescence generated by cancer cells was measured over the course of the disease. The increase in photon flux values is a well established correlate of tumour growth in vivo [25, 42].The experiments were performed in accordance with a protocol approved by the CNIO, Instituto de Salud Carlos III and Comunidad de Madrid Institutional Animal Care and Use Committee. Athymic nu/nu (Harlan) mice of 4-6 weeks of age were used. Brain colonization assays were performed by injecting 100 μl PBS into the left ventricle containing 100,000 cancer cells. Anesthetized mice (isofluorane) were injected retro-orbitally with d-luciferin (150 mg/kg) and imaged with an IVIS Xenogen machine (Caliper Life Sciences). Bioluminescence analysis was performed using Living Image software, version 3.

Cell culture. H2030-BrM3 (abbreviated as H2030-BrM) was cultured in RPMI1640 media supplemented with 10% FBS, 2 mM l-glutamine, 100 IU ml^{-1} penicillin/ streptomycin and 1 mg ml^{-1} amphotericin B.

Statistical analysis. In Figure 1, the linear regressions of the log (MTV) versus log (TLA) data to construct the scaling laws were performed using the Matlab Statistics and Machine Learning toolbox command `fitlm`. In Figure 2, the nonlinear fittings were carried out by fixing the optimum β for all patients of the same cancer type allowing only for the personalization of the growth parameter α. This approach substantially reduced the number of free parameters. Thus,

Under Review

for every set of N patients with the same cancer type having a total of $M(>3N)$ data points we fitted the N values of α. For each cancer type, the value for β that was used was the one providing the smallest mean squared error. To fit the longitudinal tumour volumetric dynamics to the model (1) with different values for $\beta = 3/4, 1, 5/4$ and optimum we used least squares. The optimization procedure was performed employing Matlab (R2016b, The MathWorks, Inc., Natick, MA, USA) function `fmincon`.

The Harrell's concordance index (c-index) [43] was computed to evaluate the model's capacity to discriminate patient subgroups with different survival. We computed the c-index for each possible threshold α in the scaling law $\log \mathrm{TLA} = \log(\alpha) + \frac{5}{4} \log \mathrm{MTV}$ or the metabolic variables (TLA, MTV) splitting the patient population into two groups (values above and below the line) and searched for the non-isolated significant values ($p < 0.1$) obtaining the highest value of the c-index. Kaplan-Meier curves were constructed to compare both populations and the log-rank two-tailed test used to compute the c-index. When either no curves with $p < 0.1$ were found or the best c-index obtained was below the value 0.7, the variable under study was considered to be unable to classify patients accurately in terms of survival.

Mesoscale tumour growth simulator. To perform the simulations, we defined 3D spatial grids of up to $80 \times 80 \times 80$ cubic voxels, each unit having 1 mm^3, in line with typical voxel sizes available in high spatial resolution morphological imaging. Thus, our computational volume was 512 cm^3, enough to explore tumour sizes from undetectable to life-incompatible in some tumour types. The basic cellular agents were clonal populations. A given clonal population could gain or lose cells depending on different biological processes incorporated into the mathematical model: mitosis, migration, cell death or trait variations due to either phenotype changes or mutations. Cells in the same subpopulation behave in the same way, except for intrinsic noise resulting in stochastic transitions. We considered four genotypes, differing in their proliferation and apoptotic rates. Initially, in all simulated scenarios, only a single genotype (genotype 1) was occupying the central voxel of the grid. At each time step, cells could proliferate, die, migrate and/or mutate, mimicking the behaviour of a tumour. For mitosis, we calculated at each iteration the number of cells undergoing proliferation, according to a probability P_{rep}. This probability was estimated to be proportional to the ratio between the current population inside the voxel and its carrying capacity (maximum number of cells it could accommodate). Each single cell attempting to divide was regarded as a Bernoulli experiment, with two possible outcomes: division (with probability P_{rep}) or not (with probability $1-P_{\mathrm{rep}}$). As a clonal population is made up of N cells, N repetitions of the same Bernoulli experiment will follow a binomial distribution. Thus, newborn cells were randomly sampled from a binomial distribution with parameters $n = N$ and $p = P_{\mathrm{rep}}$. For apoptosis, at each time step, we calculated how many dead cells an isogenic subpopulation had produced according to a given probability P_{death}, which decreased for increasing genotype number (from 1 to 4). The number of cells undergoing death was randomly sampled from a binomial distribution, in a similar way as in a proliferation event. For migration, at each time step, we computed the discrete Laplacian operator, which involved a cell gradient between a given voxel and the surrounding ones (von Neumann neighbourhood, six surrounding voxels in a 3D regular mesh). In this way we estimated which were the less populated voxels compared to the considered one. According to a given probability P_{mig}, we calculated how many cells were migrating, and how many would distribute within the neighbouring voxels. The number of cells migrating to each adjacent voxel was obtained by a random sampling of a multinomial distribution with parameters $n = N$, and six probabilities p_i being proportional to the cell gradient between adjacent voxels. Finally, mutation was modelled as a Markov chain. Cells having the genotype 1 could mutate into genotypes 2 or 3, but genotype 4 was only accessible through these two. For simplicity, the mutation probabilities were equal for all genotypic transitions. If a mutation event was successful, then a cell having the new genotype remained inside the same voxel during that time step. The temporal evolution of the tumour proliferation activity was obtained as a ratio between the difference of the total cell population at the latest time step and the previous time step divided by the duration of the time step. This method allows to both have realistic cell based dynamical rules, as in on-lattice individual-based models, but at the same time we can reach realistic tumour sizes with a high but achievable computational cost. The simulator was implemented in Julia (version 1.1.1). Simulations were performed on a network of 12-core 64 GB memory 2.7 GHz Mac Pro and 12-core 128 GB memory 2.0 GHz iMac Pro machines. Computational cost per simulation was about 2 hours per run in single-processor mode. A more detailed description of the mesoscale simulator is provided in the Supplementary Information Section S3.

References

34. Clark, K. et al. The cancer imaging archive (TCIA): maintaining and operating a public information repository. *J of Dig Imag* **26,** 1045-1057 (2013).
35. Vallières, M. et al. Radiomics strategies for risk assessment of tumour failure in head-and-neck cancer. *Sci. Rep.* **7,** 10117 (2017).
36. Kostakoglu, L. et al. A phase II study of 3'-Deoxy-3'-18F-Fluorothymidine PET in the assessment of early response of breast cancer to neoadjuvant chemotherapy: results from ACRIN 6688. *J. Nucl. Med.* **56,** 1681-1689 (2015).
37. Detterbeck, F. C., Boffa, D. J., Kim, A. W., Tanoue, L. T. The eighth edition lung cancer stage classification. *Chest* **151,** 193-203 (2017).
38. Soret, M., Bacharach, S. L., Buvat, I. Partial-volume effect in PET tumor imaging. *J. Nucl. Med.* **48,** 932-945 (2007).
39. Kass, M., Witkin, A. & Terzopoulos, D. Snakes: active contour models. *Int. J. Comput. Vis.* **1,** 321-331 (1987).
40. Zaidi, H. & El Naqa, I. PET-guided delineation of radiation therapy treatment volumes: a survey of image segmentation techniques. *Eur. J. Nucl. Med. Mol. Imaging* **37,** 2165-2187 (2010).
41. Pallud, J. et al. Prognostic value of initial magnetic resonance imaging growth rates for world health organization grade II gliomas. *Ann. Neurol.* **60,** 380-383 (2006).
42. Valiente M. et al. Serpins promote cancer cell survival and vascular co-option in brain metastasis. *Cell* **156,** 1002-1016 (2014).
43. Harrell, F. E. et al. Evaluating the yield of medical tests. *JAMA-J. Am. Med. Assoc.* **247,** 2543-2546 (1982).

Draft

Supplementary information for "Universal scaling laws rule explosive growth in human cancers"

Víctor M. Pérez-García[1]*, Gabriel F. Calvo[1], Jesús J. Bosque[1], Odelaisy León-Triana[1], Juan Jiménez[1], Julián Pérez-Beteta[1], Juan Belmonte-Beitia[1], Manuel Valiente[2], Lucía Zhu[2], Pedro García-Gómez[2], Pilar Sánchez-Gómez[3], Esther Hernández-San Miguel[3], Rafael Hortigüela[3], Youness Azimzade[4], David Molina-García[1], Álvaro Martínez[1,5], Ángel Acosta-Rojas[6], Ana Ortiz de Mendivil[7], Francois Vallette[8], Philippe Schucht[9], Michael Murek[9], María Pérez-Cano[1], David Albillo[10], Antonio F. Honguero Martínez[11], Germán A. Jiménez Londoño[12], Estanislao Arana[13] & Ana M. García Vicente[12]

[1]Mathematical Oncology Laboratory, Universidad de Castilla-La Mancha, Spain; [2]Brain Metastasis Group, Spanish National Cancer Research Centre (CNIO), Madrid, Spain; [3]Neuro-oncology Unit, Health Institute Carlos III-UFIEC, Madrid, Spain; [4]Department of Physics, University of Tehran, Iran; [5]Department of Mathematics, Universidad de Cádiz, Spain; [6]Department of Radiation Oncology, Sanchinarro University Hospital, HM Hospitales, Spain; [7]Department of Neuroradiology, Sanchinarro University Hospital, HM Hospitales, Spain; [8] Inserm U1232, Centre de Recherche en Cancérologie et Immunologie Nantes-Angers, Nantes, F-44007, France; [9]Neurosurgery Clinic, Bern Insespital, Switzerland; [10]Radiology Unit, MD Anderson Cancer Center, Madrid, Spain; [11]Thoracic Surgery Unit, Hospital General Universitario de Albacete, Spain; [12]Nuclear Medicine Unit, Hospital General Universitario de Ciudad Real, Spain; [13]Fundación Instituto Valenciano de Oncología, Spain.

*Corresponding author: victor.perezgarcia@uclm.es

20 March 2020

S1. Allometric scaling equation

We begin by considering the metabolic rate of a tumour to be $B \propto V^{\beta}$, where V is the total volume occupied by viable cells and $\beta > 0$ is the scaling exponent. Due to energy conservation, the temporal dynamics of tumour growth is given by $B = aV + b\frac{dV}{dt}$, where the first and second right-hand terms represent cell maintenance and proliferation, respectively [1]. The resulting first-order differential equation describing the time variation of $V = V(t)$ can thus be written as

$$\frac{dV}{dt} = -\gamma V + \alpha V^{\beta}, \tag{S1}$$

with $\gamma > 0$ and an initial condition for the tumour volume at time $t = t_0$, $V(t_0) = V_0$. This is a Bernoulli-type ordinary differential equation (ODE) when $\beta \neq 1$. The substitution $z(t) = V^{1-\beta}$ transforms (S1) into a linear ODE

$$\frac{dz}{dt} = (1-\beta)(\alpha - \gamma z), \tag{S2}$$

which can be solved exactly. The solution in closed form for $V(t)$ is

$$V(t) = \left[\frac{\alpha - \left(\alpha - \gamma V_0^{1-\beta}\right) e^{\gamma(\beta-1)(t-t_0)}}{\gamma}\right]^{1/(1-\beta)}. \tag{S3}$$

If $\beta > 1$, Eq. (S3) blows up in a finite time t_{crit} given by

$$t_{\text{crit}} = t_0 + \frac{1}{(\beta-1)\gamma} \log\left(\frac{\alpha}{\alpha - \gamma V_0^{1-\beta}}\right). \tag{S4}$$

The case $\alpha - \gamma V_0^{1-\beta} < 0$ corresponds to initial data with tumours having nutrient demands exceeding the supplies, thus we focus on the case $\alpha - \gamma V_0^{1-\beta} > 0$.

For highly aggressive tumours the contribution of the term $-\gamma V$, associated with cell death, is much smaller than that of proliferation. Hence, neglecting such a linear term, which is equivalent to letting $\gamma \to 0$, reduces (S3) and (S4), respectively, to the formulas used in the main text of the work

$$V(t) = \left[V_0^{1-\beta} - \alpha(\beta-1)(t-t_0)\right]^{1/(1-\beta)}, \tag{S5}$$

$$t_{\text{crit}} = t_0 + \frac{V_0^{1-\beta}}{(\beta-1)\alpha}. \tag{S6}$$

S2. Derivation and analysis of the continuous volume-dependent proliferation-rate model

S2.1. Introduction

Here we shall both provide a derivation and study in some detail the dynamics of the continuous spatio-temporal model

$$\frac{\partial u}{\partial t} = D\nabla^2 u + (\rho_0 + \rho_1 N(t))\left(1 - \frac{u}{K}\right)u, \tag{S7}$$

where $u = u(\mathbf{x}, t)$ is the tumour cell density, which is a function of space $\mathbf{x}$ and time t. The parabolic equation (S7) represents a non-local extension of the well-known Fisher-Kolmogorov partial differential equation [2]. The first term on the right-hand side of (S7) accounts for tumour cell migration that results in invasion of the surrounding tissue, with $D > 0$ denoting a characteristic cell diffusion constant. The second term on the right-hand side of (S7) reflects tumour cell proliferation. Here, $\rho_0 > 0$ and $\rho_1 \geq 0$ are the size-independent and size-dependent effective proliferation rates, respectively. When $\rho_1 = 0$, the standard (local) Fisher-Kolmogorov equation is recovered. If, however, $\rho_1 > 0$, Equation (S7) becomes non-local because it depends on the total number of cells

$$N(t) = \int_{\Omega} u(\mathbf{x}, t)\, d^3\mathbf{x}, \tag{S8}$$

with Ω denoting a sufficiently large volume containing the full tumour over its entire development, or the whole $\mathbb{R}^d$, where d

is the spatial dimension ($d = 1, 2$, or 3). This model adds spatial information with respect to the previous model (S1) and regards that the total proliferation rate may depend on tumour size, on the grounds that a larger tumour will lead to higher accumulated mutational events.

Equation (S7) is supplemented with homogeneous Neumann boundary conditions (no cell flux) $\partial u/\partial \mathbf{n} = 0$, $\forall \mathbf{x} \in \partial\Omega$, where $\mathbf{n}$ is the vector normal to the boundary $\partial\Omega$, together with an initial condition $u(\mathbf{x}, t = t_0) = u_0(\mathbf{x})$, which represents the tumour cell-density distribution at some instant $t = t_0$. In our simulations, $u_0(\mathbf{x})$ was initially assumed to be very small and highly localized (e.g. a carcinoma *in situ*), so as to describe an emergent tumour that unfolds in time.

One key dynamical quantity to be analysed later on is the total proliferation activity (or metabolic rate) which, in the context of the above model (S7), can be defined as

$$M(t) = \frac{dN}{dt} = (\rho_0 + \rho_1 N(t)) \int_\Omega \left(1 - \frac{u}{K}\right) u \, d^3\mathbf{x}. \qquad \text{(S9)}$$

The right-hand side of this expression readily follows from integrating (S7) over the domain Ω and imposing the Neumann boundary conditions.

It will also be convenient to introduce unitless time $\tau = \rho_0 t$ and space $\boldsymbol{\xi} = \sqrt{\rho_0/D}\,\mathbf{x}$ variables, together with a normalised cell density $u(\boldsymbol{\xi}, \tau) \equiv u/K$. Hence, (S9) reads as

$$M(\tau) = (1 + \eta N(\tau)) \int_\Omega (1 - u)\, u \, d^3\boldsymbol{\xi}, \qquad \text{(S10)}$$

where $\eta = \rho_1 K D^{d/2}/\rho_0^{(d+2)/2}$. Thus, the non-local Fisher-Kolmogorov equation (S7) can be cast as a one-parameter model, which makes its formal analysis simpler.

For sufficiently long times, the angular dependencies of the solutions of the FK equation become negligible with respect to the distance variable. To identify the underlying scalings of (S7), it suffices to focus on the radial dependence in u. Thus, in (S10), the differential element reduces to $d^3\boldsymbol{\xi} = B^{(d)}\xi^{d-1}d\xi$, where $B^{(1)} = 2$, $B^{(2)} = 2\pi$ and $B^{(3)} = 4\pi$, with $\xi \in [0, \infty)$ being the radial variable.

S2.2. Derivation of the non-local Fisher-Kolmogorov model

We begin by considering the tumour cell population to be structured both by its spatial position vector $\mathbf{x} \in \Omega \subset \mathbb{R}^d$ and by a net proliferation rate $\rho \in [0, \rho_{\max}]$, where $\rho_{\max}$ represents a maximum proliferation rate (for practical purposes it can be taken sufficiently large since it does not restrict our analysis). Let $w = w(\mathbf{x}, \rho, t)$ denote a cell density function such that $w(\mathbf{x}, \rho, t)d^3\mathbf{x}d\rho$ is the number of tumour cells that, at time t, have a proliferation rate ρ at point $\mathbf{x}$. We describe the dynamics of $w(\mathbf{x}, \rho, t)$ via the following migration-selection-mutation integro-differential equation:

$$\begin{aligned}\frac{\partial w}{\partial t} &= D_{\rm m}(\rho)\nabla^2 w + D_\rho \frac{\partial^2 w}{\partial \rho^2} \\ &+ \left(\rho + \nu \int_\Omega \int_0^{\rho_{\max}} \rho' \mathcal{M}(\rho, \rho') w(\mathbf{x}', \rho', t) d^3\mathbf{x}' d\rho'\right) \\ &\times \left(1 - \frac{1}{K}\int_0^{\rho_{\max}} w(\mathbf{x}, \rho', t) d\rho'\right) w(\mathbf{x}, \rho, t)\,. \qquad \text{(S11)}\end{aligned}$$

The first term on the right-hand-side accounts for cell migration with a diffusion constant $D_{\rm m}(\rho)$ that generally depends on the proliferation rate of that cell subpopulation. The second term captures the effect of non-genetic instability, which is mediated by fluctuations in the proliferation phenotype that take place with a diffusion rate D_ρ. The proliferation phenotype is a hallmark in tumours resulting from alterations in growth regulation [3]. The third term consists of two main factors. The first factor comprises selection plus the effect of genetic mutations. Those cells with a larger ρ will tend to have a fitness advantage unless exogenous mechanisms exert a detrimental action on such cells. The kernel $\mathcal{M}(\rho, \rho')$ represents the probability that the mutation of a cell with proliferation rate ρ' gives rise to a daughter cell having a proliferation rate ρ. For a genetic change to occur it is necessary a proliferative event, which explains the presence of ρ' in the integral. Notice also that an integration over all cells experiencing a mutation resulting in a proliferation rate ρ is taken weighted by the positive constant ν. Such an integration reflects the collective impact of the tumour microenvironment in promoting genetic mutations. The second factor corresponds to cell saturation with a carrying capacity K (maximum number of cells per unit volume), avoiding arbitrarily large densities.

Upon integration of (S11) over ρ and making use of the mean value theorem for integrals, together with $\int_0^{\rho_{\max}} w(\mathbf{x}, \rho, t)d\rho = u(\mathbf{x}, t)$, we get the following expressions

$$\int_0^{\rho_{\max}} \left(\frac{\partial w}{\partial t}\right) d\rho = \frac{\partial u}{\partial t}, \qquad \text{(S12)}$$

$$\int_0^{\rho_{\max}} \left(D_{\rm m}(\rho)\nabla^2 w\right) d\rho = D\nabla^2 u, \qquad \text{(S13)}$$

$$\int_0^{\rho_{\max}} \left(D_\rho \frac{\partial^2 w}{\partial \rho^2}\right) d\rho = D_\rho \frac{\partial w}{\partial \rho}\bigg|_0^{\rho_{\max}}, \qquad \text{(S14)}$$

$$\int_0^{\rho_{\max}} \rho w(\mathbf{x}, \rho, t) d\rho = \rho_0\, u(\mathbf{x}, t), \qquad \text{(S15)}$$

where D and ρ_0 denote positive characteristic cell diffusion constant and size-independent proliferation rate, respectively. If we further impose zero-flux boundary conditions on (S14), then this contribution vanishes. Also,

$$\begin{aligned}&\int_0^{\rho_{\max}} \left(\int_\Omega \int_0^{\rho_{\max}} \rho' \mathcal{M}(\rho, \rho') w(\mathbf{x}', \rho', t) d^3\mathbf{x}' d\rho'\right) w(\mathbf{x}, \rho, t) d\rho \\ &= \int_\Omega \int_0^{\rho_{\max}} \rho' w(\mathbf{x}', \rho', t) d^3\mathbf{x}' d\rho' \\ &\times \left(\int_0^{\rho_{\max}} \mathcal{M}(\rho, \rho') w(\mathbf{x}, \rho, t) d\rho\right) \\ &= u(\mathbf{x}, t) \int_\Omega \int_0^{\rho_{\max}} \rho' \mathcal{M}(\rho^*, \rho') w(\mathbf{x}', \rho', t) d^3\mathbf{x}' d\rho' \\ &= \rho_1\, u(\mathbf{x}, t) \int_\Omega u(\mathbf{x}', t) d^3\mathbf{x}' = \rho_1\, u(\mathbf{x}, t) N(t), \qquad \text{(S16)}\end{aligned}$$

where $\rho_1 \geq 0$ is a characteristic size-dependent proliferation rate. By combining the above expressions in (S11) we finally arrive at the non-local Fisher-Kolmogorov equation (S7). Notice that in the absence of mutations, which would correspond to $\mathcal{M}(\rho, \rho') = 0$, we recover the standard (local) FK equation.

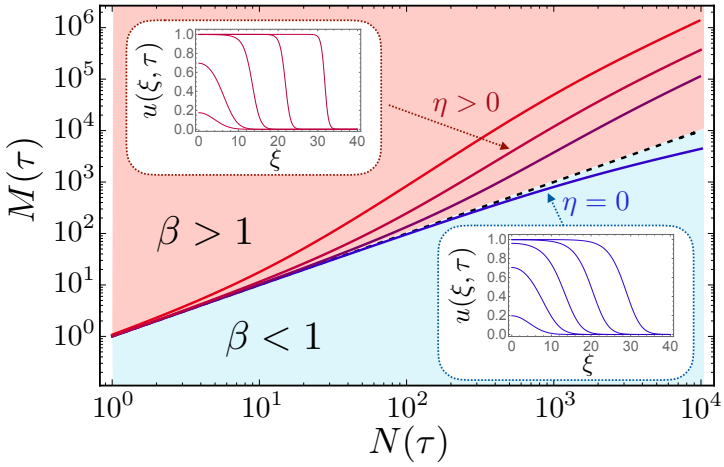

Figure S1 Local and non-local Fisher-Kolmogorov models lead to different allometric scaling laws. The main plot represents the dependence of the metabolic rate $M(\tau)$ versus the total tumour cell number $N(\tau)$. The lines represent trajectories $(M(\tau), N(\tau)$ obtained from numerical simulations of Eq. (S7) and different values of the dimensionless parameter η. The shadings indicate the exponents in each region, light blue $\beta < 1$, coral $\beta > 1$. Simulations with $\eta = 0$, corresponding to the local Fisher-Kolmogorov equation, provide a sublinear exponent $\beta = 2/3$ (blue line). Travelling wave solutions develop from the initial data with a fixed profile and interface width during propagation (bottom right inset). Simulations with different values of $\eta > 0$ (non-local FK equation) show superlinear behaviour with β close to 4/3, for sufficiently long times τ. The upper left inset shows the sharpening profiles indicating the acceleration of the front. The black dashed line marks the $\beta = 1$ threshold separating sublinearity from superlinearity.

S2.3. Allometric scaling laws in the non-local Fisher-Kolmogorov model are bounded from above by a superlinear scaling law with $\beta \leq 2$

The solution $u(\boldsymbol{\xi}, \tau)$ of the non-local Fisher-Kolmogorov equation satisfies $0 \leq u \leq 1$ everywhere. This implies that $(1-u)\,u \leq u$. It then follows from (S10) that the metabolic rate is equal to

$$\begin{aligned} M(\tau) &= (1+\eta N(\tau)) \int_\Omega (1-u)\,u\,d^3\boldsymbol{\xi} \\ &\leq (1+\eta N(\tau)) \int_\Omega u\,d^3\boldsymbol{\xi} \\ &= N(\tau) + \eta N^2(\tau). \end{aligned} \tag{S17}$$

As a consequence, the non-local Fisher-Kolmogorov model is bounded from above by an allometric scaling with exponent $\beta \leq 2$ if $\eta > 0$. Thus, (S17) provides a supersolution for (S9) given by

$$N_{\text{sup}}(\tau) = \frac{N_0 e^{\tau-\tau_0}}{1+\eta N_0 - \eta N_0 e^{\tau-\tau_0}}, \tag{S18}$$

where N_0 is the number of tumour cells at $\tau = \tau_0$. From (S18), an upper bound for the blow-up time is given by

$$\tau_{\text{crit}} = \tau_0 + \log\left(\frac{1+\eta N_0}{\eta N_0}\right). \tag{S19}$$

This time decreases as η increases.

S2.4. Allometric scaling laws in the local Fisher-Kolmogorov model are sublinear

We wish to find under what conditions there is a scaling relation between $M(\tau)$ and $N(\tau)$ (or equivalently the tumour volume) displaying a superlinear exponent (i.e. $\beta > 1$). It is instructive to first briefly examine the local Fisher-Kolmogorov equation. If $\eta = 0$ (which occurs when $\rho_1 = 0$), then (S10) reduces to

$$M_{\text{FK}}(\tau) = B^{(d)} \int_0^\infty \xi^{d-1}\,(1-u)\,u\,d\xi \equiv B^{(d)} I_{\text{FK}}^{(d)}(\tau). \tag{S20}$$

For sufficiently long times τ, the solution to the d-dimensional local Fisher-Kolmogorov equation satisfies $u \simeq 1$ up to the wave front, which propagates with a stable and invariant profile whose position (at half height) is $\xi_{\text{FK}}(\tau)$, while its width is a constant $2\sigma_{\text{FK}}$ (that may generally depend on d). For $\xi \gg \xi_{\text{FK}}(\tau)$, $u \simeq 0$. The bottom right inset in Figure S1 depicts the numerical solution of the local Fisher-Kolmogorov equation in 3D. The wave front tends to move with a constant velocity equal to 2 (or $2\sqrt{D\rho_0}$ in the original units).

The integral $I_{\text{FK}}^{(d)}(\tau)$ in (S20) can be accurately approximated by

$$\begin{aligned} I_{\text{FK}}^{(d)}(\tau) &\simeq \frac{1}{4d}\left[(\xi_{\text{FK}}(\tau)+\sigma_{\text{FK}})^d - (\xi_{\text{FK}}(\tau)-\sigma_{\text{FK}})^d\right] \\ &\simeq \frac{\xi_{\text{FK}}^{d-1}(\tau)\sigma_{\text{FK}}}{2}, \end{aligned} \tag{S21}$$

provided that $\xi_{\text{FK}}(\tau) \gg \sigma_{\text{FK}}$, which is satisfied asymptotically. Moreover, over the long time-scale, total cell number can be approximated by

$$N_{\text{FK}}(\tau) \simeq B^{(d)} \int_0^\infty \xi^{d-1} u(\xi,\tau)\,d\xi \simeq \frac{B^{(d)}\xi_{\text{FK}}^d(\tau)}{d}. \tag{S22}$$

Combining (S21) and (S22) into (S20) we get the following relation between metabolic rate and total cell number when the dynamics is governed by a d-dimensional local Fisher-Kolmogorov equation

$$M_{\text{FK}}(\tau) \simeq \frac{B^{(d)}\sigma_{\text{FK}}}{2}\left(\frac{N_{\text{FK}}(\tau)d}{B^{(d)}}\right)^{(d-1)/d}. \tag{S23}$$

This last expression shows that, within a d-dimensional local Fisher-Kolmogorov model, the allometric scaling law is sublinear, because the exponent $\beta = \frac{d-1}{d} < 1$. Hence, there cannot be explosive tumour growth in this scenario.

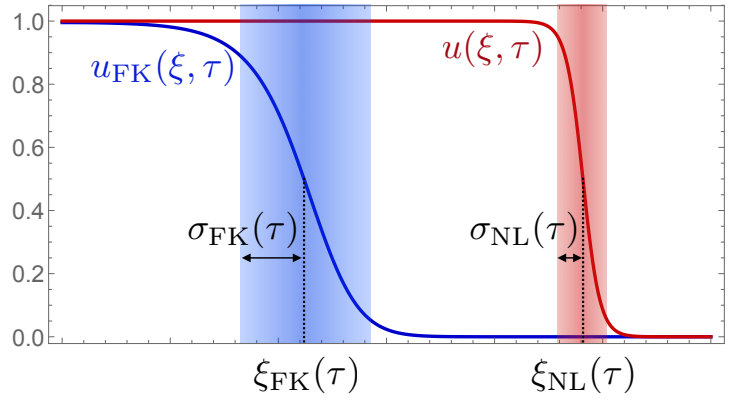

Figure S2 The solution to the non-local Fisher-Kolmogorov model accelerates with respect to the local solution and its width decreases. Comparison of the full solution $u(\xi,\tau)$ to the non-local Fisher-Kolmogorov and the local solution $u_{\rm FK}(\xi,\tau)$. The wave front positions (at half height) and half widths are $\xi_{\rm NL}(\tau)$, $\xi_{\rm FK}(\tau)$, $\sigma_{\rm NL}(\tau)$ and $\sigma_{\rm FK}(\tau)$, respectively.

S2.5. The Allometric scaling law in the 3D nonlocal Fisher-Kolmogorov model is superlinear

Let us now turn to the full non-local Fisher-Kolmogorov model where $\eta > 0$ (i.e. $\rho_1 > 0$). To gain insight, we refer to the upper left inset in Figure S1. Our numerically calculated profiles for $u(\xi,\tau)$ show that, as the wave front progresses, the velocity increases and the steepness grows without bound, tending towards a shock wave.

We will follow the same rationale as in the previous subsection. For sufficiently long times τ, the full solution to the d-dimensional non-local Fisher-Kolmogorov equation satisfies $u \simeq 1$ up to the wave front, whose position (at half height) is $\xi_{\rm NL}(\tau)$ and accelerates, while its width $2\sigma_{\rm NL}(\tau)$ decreases towards zero. This means that, when comparing the wave front propagation of the solution $u_{\rm FK}$ of the local Fisher-Kolmogorov equation to the full non-local solution, it will lag behind the wave front of u for the same initial data. Figure S2 illustrates the behaviour of both solutions schematically.

Using (S10) and working again in radial variables, we have

$$\begin{aligned} M(\tau) &= (1+\eta N(\tau))B^{(d)}\int_0^\infty \xi^{d-1}\,(1-u)\,u\,d\xi \\ &\equiv (1+\eta N(\tau))B^{(d)} I^{(d)}_{\rm NL}(\tau). \end{aligned} \tag{S24}$$

The integral $I^{(d)}_{\rm NL}(\tau)$ can be approximated as $I^{(d)}_{\rm FK}(\tau)$ and its expression is given by

$$\begin{aligned} I^{(d)}_{\rm NL}(\tau) &\simeq \frac{1}{4d}\left[(\xi_{\rm NL}(\tau)+\sigma_{\rm NL}(\tau))^d - (\xi_{\rm NL}(\tau)-\sigma_{\rm NL}(\tau))^d\right] \\ &\simeq \frac{\xi^{d-1}_{\rm NL}(\tau)\sigma_{\rm NL}(\tau)}{2}, \end{aligned} \tag{S25}$$

where we have used the fact that $\sigma_{\rm NL}(\tau) \ll \xi_{\rm NL}(\tau)$.

The behaviour of the product $\xi_{\rm NL}(\tau)\sigma_{\rm NL}(\tau)$ has been studied numerically. This was done by solving Eq. (S7) numerically using a combination of finite difference schemes and Newton-Cotes quadratures. As initial data we considered small density-amplitude and localized tumours with a given Gaussian distribution $u_0(\mathbf{x})$. Our simulations revealed that $\xi_{\rm NL}(\tau)\sigma_{\rm NL}(\tau)$ tends towards a non-zero constant μ that increases with η. Therefore,

$$I^{(d)}_{\rm NL}(\tau) \simeq \frac{\mu\,\xi^{d-2}_{\rm NL}(\tau)}{2}. \tag{S26}$$

Moreover, in the long time regime, the total number of cells can be approximated by

$$N(\tau) \simeq B^{(d)}\int_0^\infty \xi^{d-1}u(\xi,\tau)\,d\xi \simeq \frac{B^{(d)}\xi^d_{\rm NL}(\tau)}{d}. \tag{S27}$$

Combining Eqs. (S26) and (S27) into (S24) we get the following relation between metabolic rate and total cell number when the dynamics is governed by the d-dimensional non-local Fisher-Kolmogorov equation

$$M(\tau) \simeq \frac{B^{(d)}\mu}{2}\,(1+\eta N(\tau))\left(\frac{N(\tau)d}{B^{(d)}}\right)^{(d-2)/d}. \tag{S28}$$

In contrast with Eq. (S23), Eq. (S28) shows that, when $d = 3$, the non-local Fisher-Kolmogorov model leads to a superlinear allometric scaling law because the dominating exponent is $\beta = \frac{4}{3} > 1$. However, for $d \leq 2$, the exponent cannot be superlinear and no blow-up occurs.

To gain additional insight of why the scaling exponent β cannot be superlinear in lower spatial dimensions, one has to take into account that when cells proliferate they need a certain amount of available space (embodied by the carrying capacity K within the NLFK model). If $d < 3$, cells reduce their *effective clustering occupancy*. That is, they would need to migrate to more distant regions thus decreasing the interaction with other competing subpopulations or else inhibit their proliferation since they saturate earlier the available space. This eventually precludes an exploding total proliferation activity $M(t)$, albeit $M(t)$ can still grow at an exponential rate for $d = 2$.

To conclude this section, we should mention that Eq. (S7) admits the following extension

$$\frac{\partial u}{\partial t} = D\nabla^2 u + \Big(\rho_0 + \rho_1 N^\lambda(t)\Big)\Big(1-\frac{u}{K}\Big)\,u, \tag{S29}$$

where $\lambda \geq 0$ is an exponent associated to the size-dependent growth. The exponent λ characterises whether the entire tumour volume contributes to an increase in proliferation, which occurs when $\lambda = 1$, or else it is related to a fractal dimension of the tumour. For instance, if $\lambda = 2/3$, only a thin layer of cells at the tumour surface would contribute to the acceleration of growth. By adapting the previous analysis, the dominating exponent $\beta = 1+\lambda-\frac{2}{d}$, meaning that only if $\lambda > 2/3$ we would expect blow-up. Moreover, the λ exponent would also reflect effects related to the irregularity of the tumour [4].

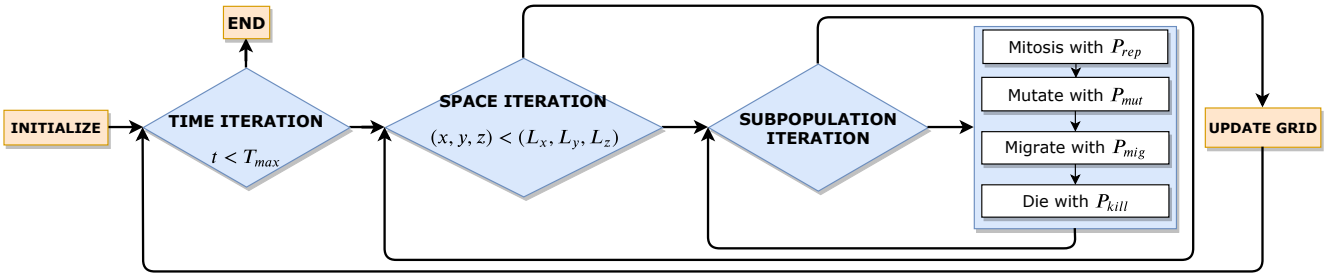

Figure S3 Model workflow scheme. Basic model outline (for implementation purposes). Initialization requires to set spatial domain and time span, to define clonal population properties, and to place initial cells in a given voxel (or several of them). After that first step, time iterations are carried out until a maximum time is reached. At each time step, every voxel is evaluated; and at each voxel, all clonal populations are updated. This updating require first the calculation how many cells are going to reproduce, migrate, mutate or die per voxel; and then all of them are updated simultaneously.

S3. Stochastic mesoscale tumour growth simulator

In order to further elucidate how different interacting cell populations influence tumour evolutionary dynamics, we developed a stochastic mesoscale tumour growth simulator. Typical cellular automata or other individual-based approaches based on cells cannot simulate tumours in volume ranges of 10–100 cm^3, that contain up to 10^{12} cells. Individual-based approaches would demand huge computational resources to simulate those amounts of cells in clinically relevant time scales (from months to several years). Thus, we opted for a different mesoscale simulation approach. By mesoscale we refer to a level of spatial detail where clinically relevant tumour sizes are reachable at the cost of cellular resolution, which is partially lost.

The model describes the spatio-temporal dynamics of several competing tumour cell subpopulations and incorporates four basic cellular processes: replication, death, migration and mutation. Cells undergo these processes at different rates, depending on the genetic/phenotypic characteristics of the clonal population they belong to. Cells in the same clonal population have the same properties, except for the microenvironmental conditions and an intrinsic noise coming from stochastic transitions. The spatial domain where these clonal populations will compete is a 3D mesh of L^3 elements (voxels). Each voxel is a compartment where many cells may coexist in each subpopulation. The size of these compartments (Δx) has been selected to resemble the voxels sizes typically available in high-resolution medical imaging (around 1 mm^3).

Instead of iterating along each cell in each voxel at every time step, whole clonal populations are evaluated at once. At each iteration, it must be determined how clonal populations change their number. This is carried out by calculating the amount of cells that duplicate, die, move to a neighbouring voxel, or mutate. By randomly sampling from binomial distributions with probabilities calculated accordingly it is possible to assess the clonal populations. To further illustrate this, we can consider a single cell attempting to divide. It will have two possible outcomes: success or failure, with excluding probabilities. This is none but a Bernoulli experiment. So, if we can draw a cell's dividing outcome by randomly sampling from a Bernoulli distribution, the outcome of a whole clonal population with N_{subpop} cells can be drawn by randomly sampling from a Binomial distribution with N_{subpop} experiments. The probabilities for each process and clonal populations are calculated at each time step inside each voxel by the equations

$$P_{\mathrm{rep}} = \frac{\Delta t}{\tau_{\mathrm{rep}}}\left(1 - \frac{N+D}{K}\right), \tag{S30a}$$

$$P_{\mathrm{mig}} = \frac{\Delta t}{\tau_{\mathrm{mig}}\Delta x^2}\left(\frac{N+D}{K}\right), \tag{S30b}$$

$$P_{\mathrm{kill}} = \frac{\Delta t}{\tau_{\mathrm{kill}}}\left(\frac{N+D}{K}\right), \tag{S30c}$$

$$P_{\mathrm{mut}} = \frac{\Delta t}{\tau_{\mathrm{mut}}}\left(\frac{N_{\mathrm{subpop}}}{K}\right), \tag{S30d}$$

where $1/\tau$ are the rates associated to a given cellular process; N and D are respectively the number of alive and dead cells in a voxel, and K is the voxel carrying capacity. The less crowded a voxel is, the more likely it will be for cells to divide, while chances of migration and death will be reduced. This leads to logistic-like growth curves for each voxel in the absence of death and interactions with other voxels. Mutation only depends on the number of cells from a given clonal population.

Mathematically, the evolution of the clonal populations is computed using the equation

$$N^{i,j,k}_{n,t+1} = N^{i,j,k}_{n,t} + N^{i,j,k}_{n_{\mathrm{rep}},t} - N^{i,j,k}_{n_{\mathrm{kill}},t} - N^{i,j,k}_{n_{\mathrm{mut}},t} + N^{i,j,k}_{n'_{\mathrm{mut}},t} - N^{i,j,k}_{n_{\mathrm{mig}},t} + N^{i',j',k'}_{n_{\mathrm{mig}},t}, \tag{S31}$$

where t is the discrete time index, n is the clonal population index, $\{i, j, k\}$ are the voxel's discrete spatial coordinates, and $\{i', j', k'\}$ represent spatial coordinates of neighbouring voxels. $N^{i,j,k}_{n,t}$ is number of cells in each clonal population n at voxel i, j, k and time t. Thus, a clonal population updates its cell number by adding to its previous state (1st right-hand term) newborn cells (2nd right-hand term), cells coming from other clonal populations that mutate into the evaluated one (5th right-hand term), and cells coming from surrounding voxels (7th right-hand term); and by subtracting dead cells (3rd right-hand term), cells mutating into a different clonal subpopulation (4th right-hand term), and cells migrating from the current voxel to surrounding ones (6th right-hand term).

Contributions are randomly sampled at each time step from binomial distributions using the probabilities (S30) and the

Model parameters			
Parameters	Description	Units	Values
L	Number of voxels per side	-	80
Δx	Voxel side length	[mm]	1
Δt	Time step length	[hours]	24
K	Carrying capacity per voxel	[cells]	$2 \cdot 10^5$
N_0	Initial population	[cells]	1
$N_{\text{threshold}}$	Minimum cell number to consider a voxel occupied	[cells]	$0.2 \cdot K$
V_{end}	Maximum tumour volume	[cm^3]	100
$1/\tau_{\text{rep}}$	Proliferation rates	[h^{-1}]	$[1.3 \cdot 10^{-3} - 5 \cdot 10^{-4}]$
$1/\tau_{\text{mig}}$	Migration rates	[h^{-1}]	$[1.7 \cdot 10^{-3} - 4 \cdot 10^{-4}]$
$1/\tau_{\text{kill}}$	Death rate	[h^{-1}]	$[1 \cdot 10^{-3} - 3.3 \cdot 10^{-4}]$
$1/\tau_{\text{mut}}$	Mutation rates	[h^{-1}]	$[1 \cdot 10^{-3} - 1 \cdot 10^{-6}]$

Table S1 Parameters of the model used for the stochastic mesoscale tumour growth simulator

Population's weights				
Process	Clonal pop. 1	Clonal pop. 2	Clonal pop. 3	Clonal pop. 4
Duplication	1	1.2	1.44	1.8
Migration	1	1.1	1.2	1.3
Death	1	0.85	0.65	0.5
Mutation	1	2	4	-

Table S2 Weights associated to each population in the simulations

equations

$$N^{i,j,k}_{n_{\text{rep}},t} \sim B\left(N^{i,j,k}_{\sum n,t}, P_{\text{rep}}\right), \tag{S32a}$$

$$N^{i,j,k}_{n_{\text{kill}},t} \sim B\left(N^{i,j,k}_{\sum n,t}, P_{\text{kill}}\right), \tag{S32b}$$

$$N^{i,j,k}_{n_{\text{mig}},t} \sim B\left(N^{i,j,k}_{\sum n,t}, P_{\text{mig}}\right), \tag{S32c}$$

$$N^{i,j,k}_{n_{\text{mut}},t} \sim B\left(N^{i,j,k}_{n,t}, P_{\text{mut}}\right). \tag{S32d}$$

A mutation (or phenotypic change) process requires defining a tree, along which cellular subpopulations can evolve as a Markov chain. Depending on whether this tree is linear, i.e. cells jump from a given clonal population to another in a stepwise way via mutation events, or branched in which cells may jump to different clonal populations from a given one, clonal populations become more aggressive as they increase the number of mutations they carry. This aggressiveness is translated into faster mitosis and migration ratios in the model; changes in these rates will be modulated by weights associated to each mutation. Migration is more intricate, as migrating cells will tend to be distributed in the surrounding voxels. Once we compute how many cells leave a voxel via (S32), their distribution (von Neumann neighbourhood, 6 surrounding voxels in 3D) is determined by randomly sampling from a multinomial distribution, whose probabilities depend on the cell gradient between voxels, mathematically

$$\begin{cases} \mathbf{N}^r_{n_{\text{mig}},t} \sim M(N^{i,j,k}_{n_{\text{mig}},t}, \mathbf{P}_{\text{dist},r}), \\ \mathbf{P}_{\text{dist},r} = \alpha \frac{N^{i,j,k}_{n,t} - N^r_{n,t}}{\sum_{r=1}^{6}\left(N^{i,j,k}_{n,t} - N^r_{n,t}\right)}, \end{cases} \tag{S33}$$

where r is one from the 6 possible neighbour voxels, and variables $\mathbf{N}^r_{n_{\text{mig}},t}$ and $\mathbf{P}_{\text{dist},r}$ (in bold font) represent vectors of r components (as many as neighbours).

Tumour volume was computed as the number of voxels that contained more than a threshold number of cells. Tumour activity was computed as the number of newborn cells at each time step.

For the simulations analyzed in this study, a cubic grid of 80 elements per side was selected, so there were 5.12×10^5 voxels available for cells to invade them. We considered four different clonal populations, each of them being more aggressive than the previous one. Cells from population 1 could mutate into populations 2 or 3, but population 4 was only accessible through these two. Initially, a single cell belonging to clonal population 1 was placed in the central voxel of the computational domain. Each voxel measured 1 mm^3, thus the maximum reachable volume for an spherical tumour that shows no boundary effects will be of 268 cm^3. Simulations were stopped once the tumour volume reached values of V_{end} = 100 cm^3.

The whole set of parameters considered in our simulations is displayed in Table S1. Additionally, the weights that modulate the different processes rates for each clonal population are shown in Table S2 as ratios compared to clonal population 1. In this paper we wanted to focus on the metabolic dynamics and the emergence of superlinear scaling laws, however the mesoscale simulator has been proven to be useful to describe the particular dynamics of specific tumour types. For instance, for glioblastomas, once the subpopulations were related to the most frequent molecular alterations/subgroups and the parameters fitted accordingly the mesoscale simulator provided a picture of the growth of these tumours resembling closely their growth dynamics. Results will be reported elsewhere.

The simulator was implemented in Julia (version 1.1.1). Simulations were performed on a network of 12-core 64 GB memory 2.7 GHz Mac Pro and a 12-core 128 GB memory 2.0 GHz iMac Pro machines. Computational cost per simulation was of about 2 hours per run in single-processor mode.

S4. Study of Partial-Volume Effects.

The term "partial-volume effect (PVE) refers to several effects that make intensity values in PET images differ from their correct values [5]. The first effect is the image blurring introduced by the spatial resolution of the imaging system. This causes spillover between regions, and leads to larger but dimmer images for small regions. Part of the signal from the source "spills out and hence is seen outside the actual source. A second source of image blurring is image sampling. The voxel contours do not match the actual contours of the tracer distribution. Thus, the signal intensity in each voxel is the mean of the intensities of the different tissues included in that voxel. In our case, and since the PVE is larger for smaller sources there could be an apparent increase in the MTVs that would be relatively larger for smaller volumes. This could result in an apparent increase of the slope of the scaling law that is difficult to quantify a priori. This is why we restricted our analysis to tumours with diameters larger than 2 cm corresponding to volumes larger than 4 cm^3. However, to exclude the PVE as potentially being the cause of the observed superlinear behaviour, we performed several computational studies.

First, we calculated the scaling exponents for two additional sets of tumours: those with diameters larger than 2.5 cm and 3.0 cm respectively. The results obtained are summarized for breast cancer in Table S3 for patients imaged with ^{18}F-FDG and Table S7 for patients imaged with ^{18}F-FLT. We also provide the results for lung cancer (Table S4), head and neck cancer (Table S5) and rectal cancer (Table S6). We excluded from the analysis gliomas since they typically contain large necrotic areas and the active tumour regions are often rim-like, thus PVE effects, if present, will not be related to the tumour diameters. For the other tumour histologies studied, having more compact shapes, there were either no or very few tumours with necrotic areas.

We did not find a reduction in the β values as the cutoff tumour size was increased, that could evidence an impact of the PVE. Instead, fluctuations in the obtained values around the original superlinear values and a trend towards a reduction of the R^2 value and an increase in the standard deviation as the number of patients was decreased were observed.

Next, we performed an additional test to assess possible PVE. Since the blurred areas around the main tumour core could be partially affected by PVE, we carried out segmentations of the core tumour areas (either manually or using the automatic segmentation algorithm with $\lambda = 0$) for a subset of the tumour histologies and compared the results with those obtained with either the automatic segmentation with ($\lambda \neq 0$) or a manual one including the lower SUV part halo around the tumour.

We performed this last study for three tumour histologies. Results for lung cancer patients imaged with ^{18}F-FDG are summarized in Table S8. There the comparison was carried out between the standard automatic procedure and the automatic procedure without the inclusion of the surrounding lower SUV values halo around the tumour core ($\lambda = 0$, see 'Methods'). The exponents obtained were superlinear with overlapping intervals. In the second series of tests, for breast cancer patients imaged with ^{18}F-FDG, we compared the results of the standard automatic segmentation with the one choosing $\lambda = 0$ and a manual segmentation performed choosing only the higher value SUV areas. Results are shown in Table S9. The three values obtained were in line with the exponent reported in the main text, and in any case showed superlinear behaviour. A final comparison was performed for the colon cancer patients for which no automatic segmentation could be performed due to the proximity of confounding structures. There, two manual segmentations were done, one of them including the whole tumour and a second one restricted to the core higher SUV value areas. Results are summarized in Table S10. The values were compatible within them and with the superlinear dynamics.

In summary, although the PVE is always present in PET images and could potentially affect the obtained scaling exponents, it appears that for our scanners and type of study the choice of a minimal tumour size of 2 cm was enough to guarantee a minor impact of this effect.

References

[1] West, G.B., Brown, J.H., Enquist, B.J. A general model for ontogenetic growth. *Nature* **413**, 628-631 (2001).

[2] Murray, J.D. *Mathematical Biology.* Third Edition. (Springer-Verlag, Berlin, 2002).

[3] Hanahan D., & Weinberg, R. A. Hallmarks of cancer: the next generation. *Cell* **144,** 646-674 (2011).

[4] Pérez-Beteta, J. et al. Tumor surface regularity at MR imaging predicts survival and response to surgery in patients with glioblastoma. *Radiology* **288,** 218-225 (2018).

[5] Soret, M., Bachrach, S.L., Buvat, I. Partial-Volume Effect in PET Tumor Imaging. *J Nucl Med* **48**, 932-945 (2007).

Dataset	Fitting exponent (β)	Std deviation	Number of patients	R^2
> 2.0 cm	1.307	0.069	54	0.87
> 2.5 cm	1.331	0.084	51	0.83
> 3.0 cm	1.211	0.124	37	0.73

Table S3 Comparison of the scaling exponent β obtained for breast cancer patients imaged with ^{18}F-FDG and different lesion size cutoff values

Dataset	Fitting exponent (β)	Std deviation	Number of patients	R^2
> 2.0 cm	1.248	0.032	175	0.90
> 2.5 cm	1.206	0.045	133	0.84
> 3.0 cm	1.261	0.064	92	0.81

Table S4 Comparison of the scaling exponent β obtained for lung cancer patients imaged with ^{18}F-FDG and different lesion size cutoff values

Dataset	Fitting exponent (β)	Std deviation	Number of patients	R^2
> 2.0 cm	1.182	0.030	76	0.87
> 2.5 cm	1.229	0.067	50	0.87
> 3.0 cm	1.300	0.097	40	0.82

Table S5 Comparison of the scaling exponent β obtained for head and neck cancer patients imaged with ^{18}F-FDG and different lesion size cutoff values

Dataset	Fitting exponent (β)	Std deviation	Number of patients	R^2
> 2.0 cm	1.386	0.152	23	0.80
> 2.5 cm	1.471	0.159	22	0.81
> 3.0 cm	1.712	0.224	20	0.76

Table S6 Comparison of the scaling exponent β obtained for rectal cancer patients imaged with ^{18}F-FDG and different lesion size cutoff values

Dataset	Fitting exponent (β)	Std deviation	Number of patients	R^2
> 2.0 cm	1.188	0.035	75	0.92
> 2.5 cm	1.147	0.046	60	0.91
> 3.0 cm	1.096	0.065	44	0.87

Table S7 Comparison of the scaling exponent β obtained for breast cancer patients imaged with ^{18}F-FLT and different lesion size cutoff values

Segmentation procedure	Fitting exponent (β)	Std deviation	Number of patients	R^2
Standard automatic	1.248	0.032	175	0.90
Only core ($\lambda = 0$) automatic	1.192	0.047	169	0.79

Table S8 Comparison of the scaling exponent β obtained for lung cancer patients imaged with ^{18}F-FDG with different segmentation procedures. The automatic algorithm failed to provide consistent results with $\lambda = 0$ for six patients and were excluded from the analysis.

Segmentation procedure	Fitting exponent (β)	Std deviation	Number of patients	R^2
Standard automatic	1.307	0.069	54	0.87
Only core ($\lambda = 0$) automatic	1.233	0.094	54	0.76
Only core (manual)	1.255	0.052	54	0.91

Table S9 Comparison of the scaling exponent β obtained for breast cancer patients imaged with ^{18}F-FDG with different segmentation procedures.

Segmentation procedure	Fitting exponent (β)	Std deviation	Number of patients	R^2
Manual (whole tumour)	1.386	0.152	23	0.80
Manual (only core)	1.307	0.137	23	0.82

Table S10 Comparison of the scaling exponent β obtained for rectal cancer patients imaged with ^{18}F-FDG with different segmentation procedures.

Extended data figures for “Universal scaling laws rule explosive growth in human cancers"

Víctor M. Pérez-García[1]*, Gabriel F. Calvo[1], Jesús J. Bosque[1], Odelaisy León-Triana[1], Juan Jiménez[1], Julián Pérez-Beteta[1], Juan Belmonte-Beitia[1], Manuel Valiente[2], Lucía Zhu[2], Pedro García-Gómez[2], Pilar Sánchez-Gómez[3], Esther Hernández-San Miguel[3], Rafael Hortigüela[3], Youness Azimzade[4], David Molina-García[1], Álvaro Martínez[1,5], Ángel Acosta-Rojas[6], Ana Ortiz de Mendivil[7], Francois Vallette[8], Philippe Schucht[9], Michael Murek[9], María Pérez-Cano[1], David Albillo[10], Antonio F. Honguero Martínez[11], Germán A. Jiménez Londoño[12], Estanislao Arana[13] & Ana M. García Vicente[12]

[1]Mathematical Oncology Laboratory, Universidad de Castilla-La Mancha, Spain; [2]Brain Metastasis Group, Spanish National Cancer Research Centre (CNIO), Madrid, Spain; [3]Neuro-oncology Unit, Health Institute Carlos III-UFIEC, Madrid, Spain; [4]Department of Physics, University of Tehran, Iran; [5]Department of Mathematics, Universidad de Cádiz, Spain; [6]Department of Radiation Oncology, Sanchinarro University Hospital, HM Hospitales, Spain; [7]Department of Neuroradiology, Sanchinarro University Hospital, HM Hospitales, Spain; [8] Inserm U1232, Centre de Recherche en Cancérologie et Immunologie Nantes-Angers, Nantes, F-44007, France; [9]Neurosurgery Clinic, Bern Insespital, Switzerland; [10]Radiology Unit, MD Anderson Cancer Center, Madrid, Spain; [11]Thoracic Surgery Unit, Hospital General Universitario de Albacete, Spain; [12]Nuclear Medicine Unit, Hospital General Universitario de Ciudad Real, Spain; [13]Fundación Instituto Valenciano de Oncología, Spain.

*Corresponding author: victor.perezgarcia@uclm.es

20 March 2020

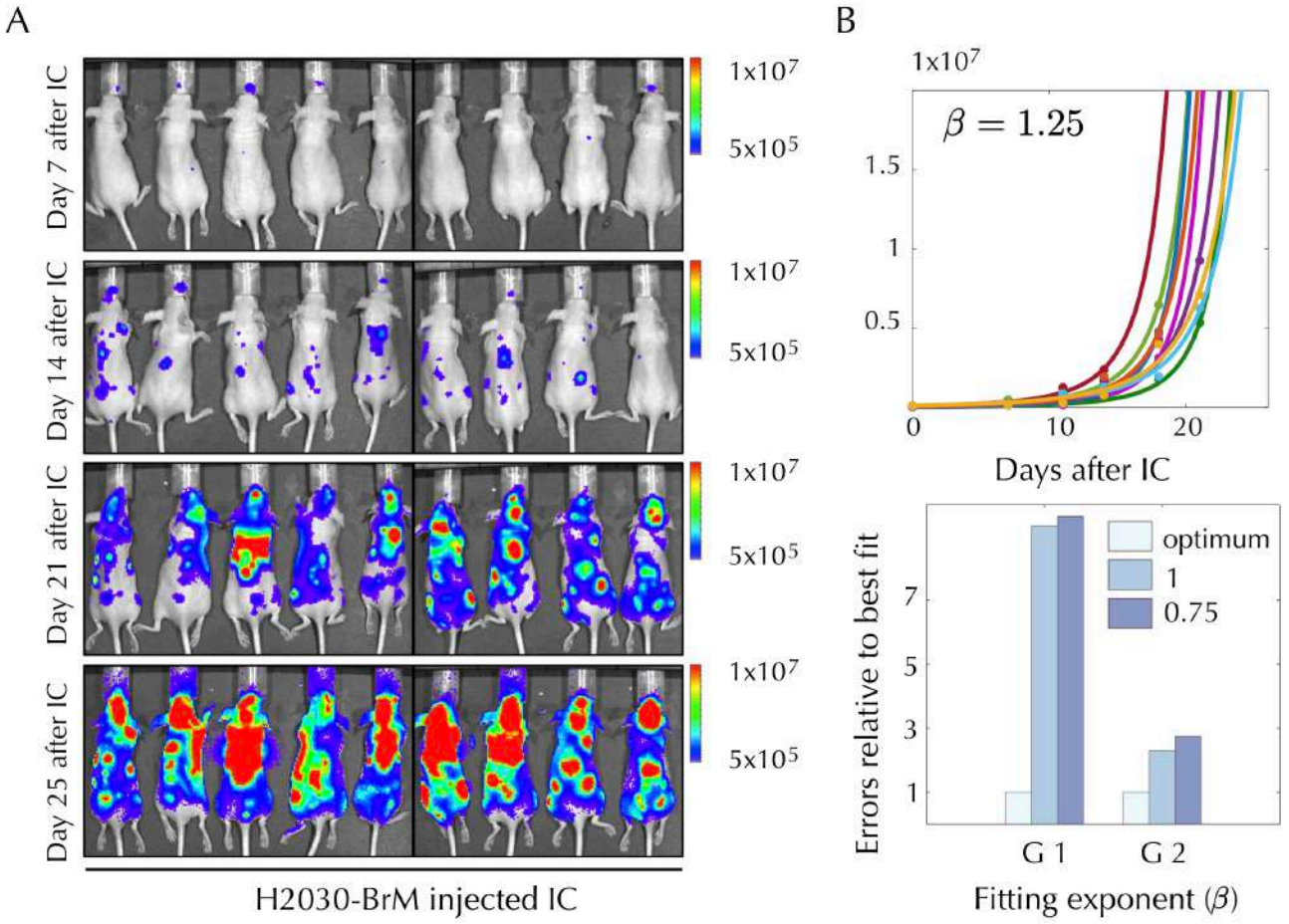

Extended Data Figure 1 Two human cancer animal models display superlinear growth dynamics. Group 1 (G1) data correspond to untreated nude mice injected with the human lung adenocarcinoma brain tropic model H2030-BrM (see methods). Group data (G2) correspond to primary glioma cells (L0627) expressing the luciferase reporter gene injected into the brain of nude mice (see methods). Bioluminiscence images for G1 for some mice are shown in panel A. Total tumour mass growth curves for G1 showed superlinear dynamics with best fitting exponent β = 1.25 (for G2 it was β = 1.3). (B, upper panel). Errors relative to best fit were found to be substantially smaller with the optimal superlinear fits than for both the linear and sublinear fits (exponents 1 and 0.75 respectively) (B, lower panel).